Preemptive glycogen storage in granulosa cells powers avascular corpus luteum via glycogenolytic energy provision

Jianning Liao[1†], Qinghua Liu[1,7†], Cong Liu[2†], Guiqiong Liu[1†], Xiang Li[1†], Xiaodong Wang[1], Yaqin Wang[2], Ruiyan Liu[1], Hao Wu[3], Chaoli Wang[5], Hongru Shi[1], Yongheng Zhao[1], Wenkai Ke[1], Zaohong Ran[1], Zian Wu[1], Bowen Tan[1], Xunping Jiang[1], Quanfeng Wang[6], Guohua Hua[1], Shujun Zhang[1], Qingzhen Xie[2*], Guoshi Liu[3*], Changjiu He[1,4*]

[1] Key Laboratory of Agricultural Animal Genetics, Breeding and Reproduction of Ministry of Education, College of Animal Sciences and Technology, Huazhong Agricultural University, Wuhan 430070, PR China;

[2] Centre for Reproductive Medicine, Renmin Hospital of Wuhan University, Wuhan 430000, China.

[3] Key Laboratory of Animal Genetics and Breeding of the Ministry of Agriculture, College of Animal Science and Technology, China Agricultural University, Beijing, China

[4] College of Animal Science and Technology, Shihezi University, Shihezi, China.

[5] Xinjiang Western Animal Husbandry Co., Ltd, Shihezi, China.

[6] Xinjiang Jinken aoqun agriculture and animal husbandry technology Co., Ltd, Hetian, China.

[7] Binzhou Bincheng District Animal Husbandry and Veterinary Service Center, Binzhou, China.

[†] These authors contributed equally to this work.

***Corresponding Author**:

Changjiu He,

Orcid ID: 0000-0002-0350-9799;

Email: chungjoe@mail.hzau.edu.cn; Huazhong Agricultural University, Wuhan 430070, China.

Guoshi Liu,

Orcid ID: 0000-0002-5688-3645;

Email: gshliu@cau.edu.cn; China Agricultural University, Beijing 100193, China

Qingzhen Xie,

Orcid ID: 0000-0002-4628-4278;

Email: rm001138@whu.edu.cn; Renmin Hospital of Wuhan University, Wuhan 430000, China.

Short title: GCs store glycogen for corpus luteum

ABSTRACT

The corpus luteum (CL) arises from the luteinization of follicular granulosa cells (GCs) and theca cells, marked by rapid progesterone elevation and angiogenesis. Intriguingly, angiogenesis lags behind progesterone elevation, creating an avascular phase during which luteal cells must fuel intensive steroidogenesis without perfusion. How the avascular CL meets this energetic demand remains a mystery. Here, we reveal a novel cellular adaptive mechanism–GC energy storage (GCES)–that resolves this enigma. We demonstrate that upon luteinization initiation, GCs enter a metabolically quiescent state yet enhance glucose uptake via SLC2A1, converting it into glycogen through the hCG (LH)-MAPK-RUNX1-Insulin signaling axis. Catabolism of this glycogen reserve supplies the energy required for the avascular CL, ensuring normal luteogenesis. GCES is evolutionarily conserved across mice, sheep and humans. Genetic or pharmacological disruption of GCES or glycogenolysis induces luteal insufficiency, whereas timely glucose administration enhances GCES, improving luteal function and optimize reproductive outcome in both mouse and ovine models. In human study, orally intake of glucose post-hCG significantly augments GCES and enhances progesterone production in women. These results advance luteal physiology by uncovering a universal reproductive principle with direct clinical implications.

Keywords: ovulation, glycogen, granulosa cell, corpus luteum, follicle, luteinization.

54 **INTRODUCTION**

55 The corpus luteum (CL) is a temporary ovarian endocrine structure critical for
56 reproduction. It sustains pregnancy by secreting progesterone and orchestrates the
57 reproductive cycle via its cyclic formation and regression [1, 2]. Luteal insufficiency,
58 defined by the suboptimal progesterone production and shortened luteal phase,
59 represents a common etiology of female subfertility and is closely linked to
60 reproductive disorders, including menstrual disorders, premenstrual spotting and
61 recurrent pregnancy loss [3, 4]. It is estimated that ~8% of reproductive-age women
62 experience luteal insufficiency, with the incidences escalating in parallel to maternal
63 age [3, 5-8]. Notably, luteal insufficiency is prevalent in recurrent miscarriage cases [9,
64 10], underscoring its profound impact on reproductive health.

65 CL arises from the luteinization of granulosa cells (GCs) and theca cells, a process
66 triggered by the pre-ovulatory surge of luteinizing hormone (LH) or human chorionic
67 gonadotropin (hCG, an LH-equivalent hormone) [11]. Luteinization encompasses
68 multiple coordinated cellular mechanisms, such as proliferation cessation,
69 steroidogenesis reprogramming, GC-layer stiffening, cell migration and
70 neovascularization [2, 12-15]. LH (hCG)-activated downstream regulators, including
71 P21CIP1, P27KIP1, ERK1/2, PI3K/AKT, CEBPα/β, RUNX1/2, NR4A2/NURR1,
72 CREB, cortisol/glucocorticoid receptors and H3K27me3/H3K9me3 [16-25],
73 collectively regulate luteinization.

74 Despite originating from GCs, luteal cells exhibit markedly elevated progesterone
75 synthesis, which outstrips the output of their GC precursors by several orders of
76 magnitude [26]. This metabolic upscaling renders the CL one of the most energetically
77 demanding tissues. Notably, the intrafollicular microenvironment remains non-
78 vascularized, necessitating *de novo* angiogenesis for efficient substance delivery to
79 luteal cells [27-29]. Paradoxically, vascularization in the nascent CL lags behind the
80 elevation in progesterone production. This temporal uncoupling of metabolic demand
81 and vascularization creates a transient avascular phase during early luteogenesis,

82 presenting a long-standing physiological enigma, i.e., how does the avascular CL meet
83 its high energetic requirements for elevated progesterone production.

84 Here, we report a novel cellular adaptive mechanism, GC energy storage (GCES),
85 which addresses this enigma. By using single-cell/spatial transcriptomics, targeted
86 metabolic flux tracing, isotope tracing, and conditional gene silencing, the results show
87 that GCs enter a metabolically quiescent state with suppressed energy expenditure upon
88 hCG (LH) stimulation. Concomitantly, these cells proactively uptake glucose via
89 SLC2A1 and convert the glucose into glycogen through MAPK/RUNX1/Insulin
90 signaling, establishing an energy reservoir. During the avascular phase, the luteinizing
91 GCs use the stored glycogen to satisfy the energy demanding of elevated progesterone
92 synthesis, thereby ensuring normal luteogenesis. GCES is evolutionarily conserved
93 across species. Disrupting GCES or glycogenolysis precipitate luteal insufficiency,
94 while enhancing GCES improves luteal function and fertility outcomes in mammals.

95 **RESULTS**

96 **1. Integrated multi-omics analysis reveals systemic metabolic downregulation GCs**
97 **during early luteinization**

98 To investigate the cellular response of GCs during the early stage of luteinization, the
99 mouse ovaries harvested at 0, 1 and 6 hours post-hCG (H0, H1 and H6) administration
100 were subjected to single-cell RNA sequencing to capture high-resolution
101 transcriptomes of ovarian cell populations (Figure S1A, B). Complementary spatial
102 transcriptomic analysis of publicly available mouse ovarian datasets [30] enabled
103 construction of a spatially informed transcriptomic atlas of GCs across follicular
104 development stages (Figure S1C). By integrating the single-cell and spatial
105 transcriptomic data (Figure 1A; see Materials and Methods), we reconstructed a high-
106 resolution and spatially informed transcriptional atlas of GCs in pre-ovulatory follicles
107 following luteinization initiation (Figure 1B; Table S1). Principal component analysis
108 (PCA) revealed significant transcriptional divergence in GCs across timepoints (Figure
109 1C), with integrated data demonstrating acceptable quality (gene training scores: ~0.8;

110 AUC: 0.63–0.70) and enhanced resolution versus original spatial data (Figure 1D-F;
111 S2).

112 Differential expression analysis identified 3000 significantly upregulated and
113 3187 downregulated genes in GCs post-hCG administration. Gene Ontology (GO)
114 analysis demonstrated that the upregulated genes predominately enriched in established
115 luteinization-associated processes, including *Cell Migration*, *Angiogenesis*, *Cell*
116 *Adhesion*, *Extracellular Matrix Organization*, *Inflammatory Response* and *etc*, aligning
117 with the observations of previous studies, however, two processes–*Response to Insulin*
118 and *Glucose Homeostasis*–were newly identified (Figure 1G).

119 Conversely, downregulated genes exhibited striking enrichment in diverse yet
120 interconnected biological processes: *Mitochondrial ATP Synthesis*, *Respiratory Chain*
121 *Complex I Assembly*, *Aerobic Respiration*, *Tricarboxylic Acid (TCA) Cycle*,
122 *Respiratory Electron Transport Chain*, *Electron Transport, NADH to Ubiquinone*,
123 *Lipid Metabolic Process*, *Fatty Acid Metabolic Process*, *Vesicle transport, ER to Golgi*,
124 *Response to ER Stress*, *Protein Folding*, *Vesicle Transport, Golgi to ER*, *Protein N-*
125 *glycan Processing*, *Protein Heterodimerization*, *ER Unfolded Protein Response*,
126 *Protein Glycosylation*, *Oligosaccharide Biosynthesis*, *Golgi Organization*, *Protein O-*
127 *linked Mannosylation*, *Protein Localization*, *Lysosomal Membrane* (Figure 1H). These
128 processes collectively implicate a metabolic reprogramming toward quiescence,
129 characterized by suppressed ATP-generating activities in mitochondria and energy-
130 demanding activities in the endomembrane system. This transcriptional shift provides
131 preliminary evidence suggesting a hitherto unrecognized cellular adaptation wherein
132 GCs adopt energy-conserving strategies during early luteinization, suppressing ATP-
133 generating and energy-consuming processes to minimize energy expenditure.

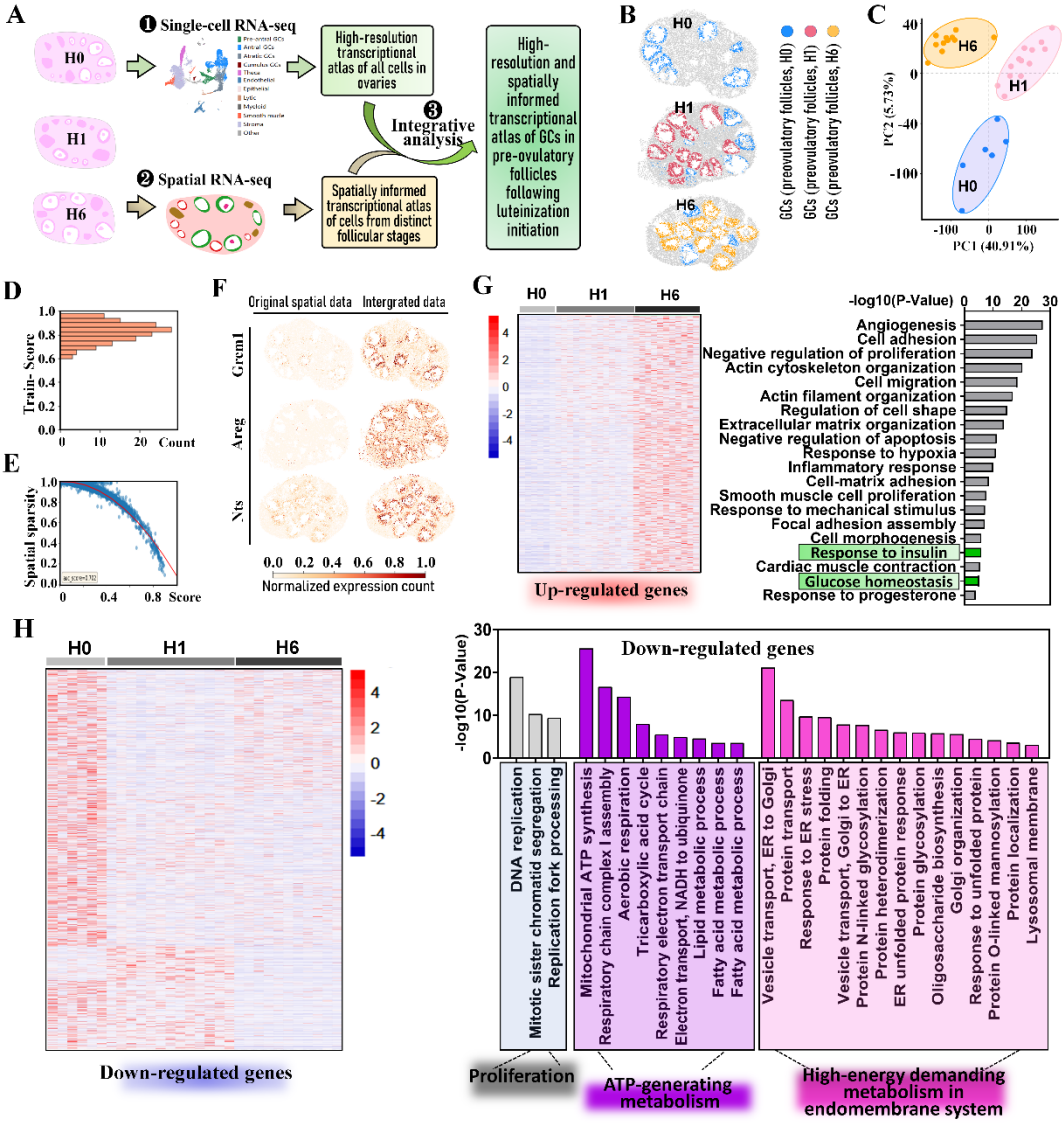

Figure 1. Integrated multi-omics analysis reveals systemic metabolic downregulation GCs during early luteinization. (A) Workflow for integrative analysis of single-cell and spatial transcriptomics data. (B) Identification of GCs in pre-ovulatory follicles at specified time points post-hCG administration using integrated analysis. (C) PCA analysis of transcriptomic differences in GCs from pre-ovulatory follicles. (D) Histogram of gene similarity scores derived from model training data. (E) Scatter plot of tangram-predicted gene scores (x-axis) versus spatial sparsity (y-axis) based on integrated transcriptome data. (F) Expression analysis of randomly selected genes demonstrated enhanced spatial resolution and clearer localization patterns in the integrated dataset compared to the original spatial transcriptomics data. (G) GO enrichment analysis of the upregulated expression cluster. Left: Heatmap of cluster-specific genes; Right: Enriched GO terms. (H) GO enrichment analysis of the downregulated expression cluster. Left: Heatmap of cluster-specific genes; Right: Enriched GO terms.

147 **2. Metabolic attenuation and bioenergetic repression in GCs characterize early**
148 **luteinization**

149 The transcriptomic predictions of bioenergetic suppression were corroborated through
150 multimodal analyses, including ^{13}C-glucose tracing, ultrastructural imaging, and
151 bioenergetic profiling. Metabolic flux analysis demonstrated diminished ^{13}C-glucose
152 labeling in glycolysis and TCA cycle intermediates following hCG administration
153 (Figure 2A, B; S3A). Ultrastructural remodeling of mitochondria was evident,
154 transitioning from rounded at H0 to elongated morphologies at H6, concomitant with
155 significant reduction in ER-mitochondrial contact sites–critical platforms for metabolic
156 crosstalk (Figure 2C) [31]. This architectural reorganization paralleled profound
157 bioenergetic suppression, characterized by a 27.0% decline in mitochondrial membrane
158 potential (MMP), a 2.90-fold increase in NAD^+/NADH ratio, and a 44.1% decrease in
159 ATP synthesis relative to H0 controls (Figure 2D-F).

160 We next validated the attenuation of metabolic activity within the endomembrane
161 system by quantitatively analyzing protein glycosylation, vesicular trafficking,
162 secretory capacity, and lysosomal biogenesis. Ultrastructural examination revealed that
163 GCs at H0 exhibited dilated endoplasmic reticulum (ER) cisternae and accumulated
164 transport vesicles adjacent to Golgi apparatus. By 6 hours post-hCG, ER tubules had
165 transformed into elongated cord-like structures, concurrent with a substantial reduction
166 in peri-Golgi vesicular density (Figure 2G). This morphological remodeling correlated
167 with the coordinated downregulation of genes regulating N-linked glycosylation,
168 oligosaccharide biosynthesis, vesicle assembly, and Golgi-specific O-glycosylation
169 (Figure S3B-D). Metabolomic profiling revealed that the intermediates in the
170 glycosylphosphatidylinositol (GPI) anchor biosynthesis pathway, a critical process in
171 glycosylation, was generally declined in H6 GCs (Figure 2H). This observation was
172 further substantiated by lectin binding assay, which demonstrated a significant
173 reduction in the abundance of glycosylated proteins post-hCG (Figure 2I; S3E).
174 Quantitative assessment of secretory capacity via secreted alkaline phosphatase (SEAP)
175 reporter transfection demonstrated a significant reduction in SEAP activity following
176 hCG (Figure 2J, K; S3F). Genes in the mannose-6-phosphate (M6P) pathway–essential

for lysosomal biogenesis–were significantly downregulated at H6 (Figure 2L), correlating with decreased LysoTracker Green fluorescence intensity (Figure 2M) and acid phosphatase activity (Figure 2N).

These data demonstrate metabolic quiescence transition in GCs during early luteinization, validating the omics predictions.

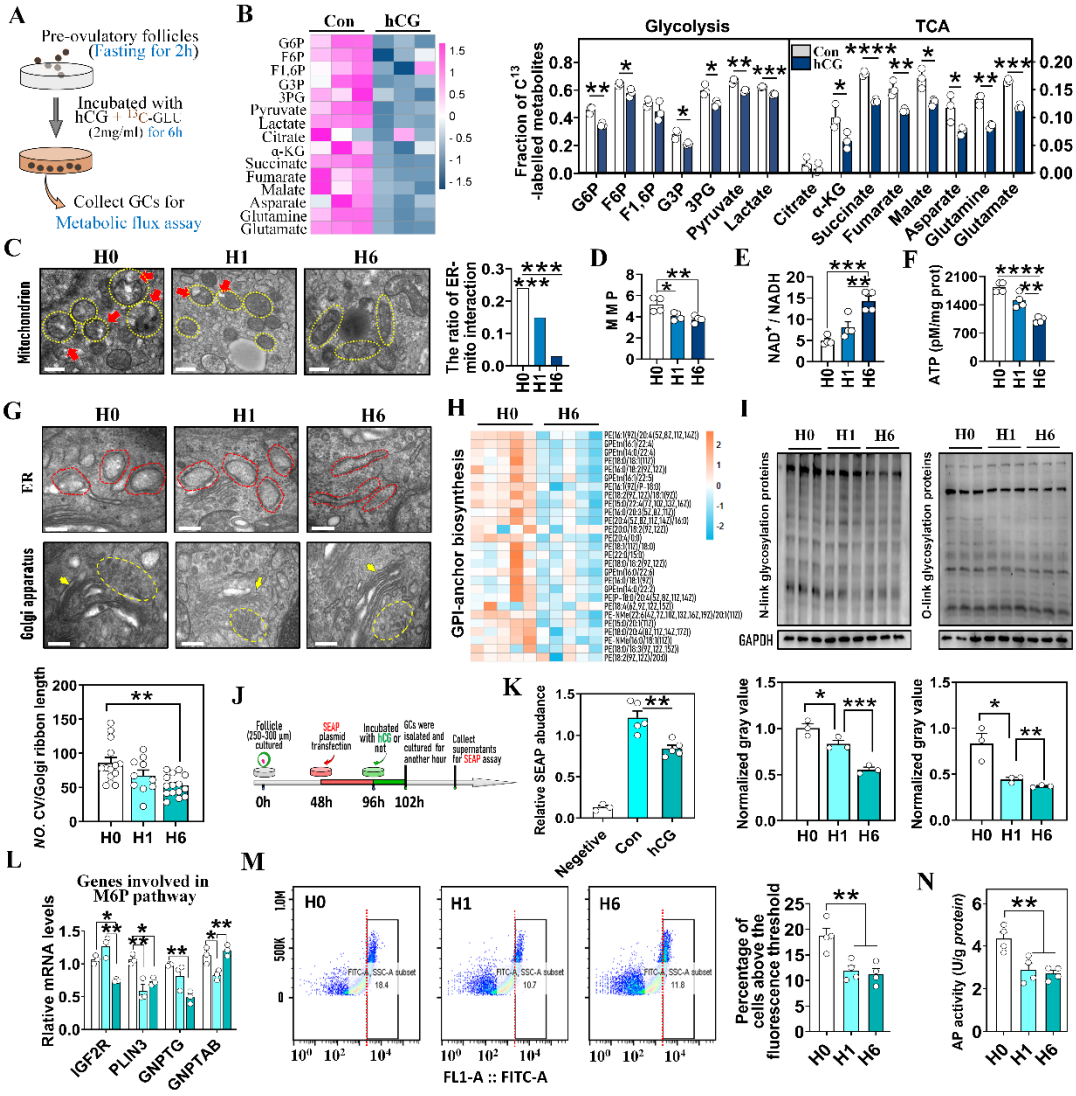

Figure 2. Metabolic attenuation and bioenergetic repression in GCs characterize early luteinization. (A) Workflow for metabolic flux analysis. Pre-ovulatory follicles were fasted for 2 hours, then cultured in luteinization medium with U-^{13}C6-glucose as sole carbon source for 6 hours before GC isolation and targeted metabolomics. (B) Quantitative analysis of ^{13}C-labeled glycolytic and TCA cycle intermediates. Left: heatmap; Right: quantification (n = 3 GC samples). The control was defined as the group cultured in hCG-free medium. (C) Changes in mitochondrial ultrastructure and ER-mitochondria contact sites following hCG injection. Left: representative images. Right: quantification. Yellow outlines: mitochondria; red arrow: contact sites. Scale bar = 500 nm. (D) MMP measured by JC-1 staining (n = 4 GC samples). (E) NAD^+/NADH ratio determined by colorimetric assay (n = 4 GC samples). (F) ATP levels measured by luciferase bioluminescence assay (n = 4 GC samples). (G) Ultrastructural changes in ER and Golgi apparatus in GCs following hCG injection. Top: representative images. Down:

quantification. Red outlines: ER; yellow arrow: Golgi apparatus; yellow outline: transport vesicles. Scale bar = 200 nm. (H) Heatmap showing changes in the content of GPI-anchor biosynthesis pathway intermediates post-hCG (n = 5 GC samples). (I) Quantification of N-linked (Concanavalin A)/O-linked glycoprotein (Peanut Agglutinin) abundance in GCs by lectin blotting. Top: lectin blot; Down: quantification (n = 3 GC samples). (J) Workflow for SEAP reporter assay. (K) Quantification of SEAP secreted into the supernatant using chemiluminescence assay (n = 5 supernatant samples). (L) Changes in M6P pathway gene expression post-hCG injection (n = 3 GC samples). (M) Flow cytometry analysis of GCs with high-intensity Lyso-tracker green fluorescence. Red line: fluorescence intensity threshold; cells right of threshold line classified as high-intensity fluorescent (n = 4 GC samples). (N) Detection of changes in lysosomal acid phosphatase activity using colorimetric assay (n = 4 GC samples). Data represent mean ± SD. Significance determined by two-tailed unpaired Student's t-test (G) and one-way ANOVA followed by Tukey's post hoc test (*P<0.05, **P<0.01, ***P<0.001, ****P<0.0001). Results shown (C-G, I-N) are from one of at least three independent replicates; all experiments produced comparable data.

3. Enhanced glucose uptake supports glycogen biosynthesis in GCs during early luteinization

Intriguingly, despite transitioning to a metabolically quiescent state, GCs at H6 exhibited a significant increase in glucose uptake compared to H0 controls (Figure 3A). Transporter expression profiling identified SLC2A1 as the predominant glucose transporter of this enhanced uptake (Figure 3B; S4A). Intracellular glucose can be directed toward ATP generation or storage as lipids or glycogen (Figure 3C) [32]. Metabolic flux analysis ruled out significant catabolic utilization (Figure 2A, B), and nor for the lipid storage since colorimetric assays revealed the reduced intracellular free fatty acids and triglycerides (Figure S4B, C). To directly assess glycogen conversion, we performed ^{13}C-glucose tracing coupled with Liquid Chromatograph-Tandem Mass Spectrometer (LC-MS/MS). hCG-treated GCs exhibited pronounced ^{13}C enrichment in glycogen (35% incorporation versus, 8% in controls; Figure 3D, E), demonstrating preferential glycogen biosynthesis. Consistent with this, Western blotting and qRT-PCR analysis detected activation of the glycogenesis pathway following hCG administration (Figure 3F; S4D). Complementary Periodic Acid-Schiff (PAS) staining and colorimetric quantification confirmed a significant elevation in glycogen content within H6 GCs (Figure 3G, H).

We next characterized the temporal dynamics of glycogen storage and its functional correlates throughout luteinization process. Integrated analysis defined distinct phases: a glycogenesis phase (H0-H9) followed by a glycogenolysis phase (H9-H15), evidenced by glycogenesis/glycogenolysis pathway protein expression (Figure

3I) and PAS staining (Figure 3J). Notably, during glycogenesis phase, ATP production declined (Figure 3K) while progesterone levels rose gradually up to 80 ng/g (Figure 3L). Upon entering glycogenolysis phase (H9-H15), ATP levels surged (Figure 3K) coincident with the peak progesterone secretion (~200 ng/g; Figure 3L). Critically, this glycogenolysis phase–characterized by high energy demand for steroidogenesis–occurred within the developing CLs prior to the establishment of internal vascularization (Figure 3M). These data might indicate GCs strategically store glycogen as an energy reservoir during early luteinization, and subsequently mobilized to fuel the intensive progesterone production required during the avascular phase.

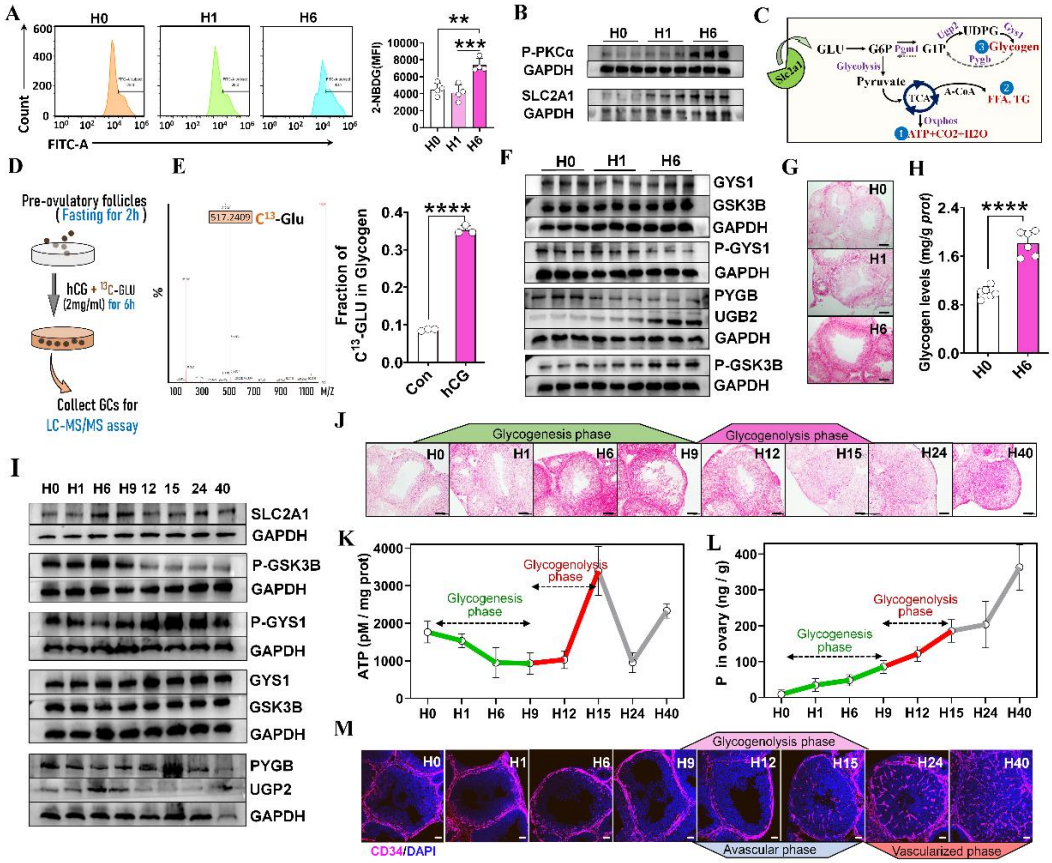

Figure 3. Enhanced glucose uptake supports glycogen biosynthesis in GCs during early luteinization. (A) Flow cytometric analysis of cellular glucose uptake capacity post-hCG injection. Isolated GCs were incubated with fluorescent analog 2-NBDG (100 μM) for 30 minutes prior to analysis. Left: representative images; Right: quantification (n = 4 GC samples). (B) Western blotting analysis of SLC2A1 and its upstream kinase P-PKCα in GCs post-hCG injection (n = 3 GC samples). (C) Schematic of intracellular glucose carbon flux. (D) ^{13}C-glucose tracing workflow. Pre-ovulatory follicles fasted 2 hours, then cultured in luteinization medium with U-^{13}C6-glucose (sole carbon source) for 6 hours before GC isolation and LC-MS/MS analysis. (E) Quantitative ^{13}C enrichment in glycogen (n = 3 GC samples). The control was defined as the group cultured in hCG-free medium. (F) Changes in glycogenesis/glycogenolysis proteins during early luteinization (n = 3 GC samples). (G) PAS staining of glycogen in GCs during early luteinization. Scale bar = 100 μm. (H) Colorimetric quantification of glycogen content (n = 6 GC samples). (I) Changes in

glycogenesis/glycogenolysis proteins throughout luteinization. (J) PAS staining of glycogen throughout luteinization. Scale bar = 100 μm. (K) ATP content changes throughout luteinization (n = 4-7 GC samples). (L) Radioimmunoassay of progesterone in ovarian homogenates throughout luteinization (n = 4-7 ovarian samples). (M) Vascularization changes assessed by $CD34^+$ endothelial cells (red) during luteinization. Nuclei counterstained with DAPI (blue). Scale bar = 50 μm. Data represent mean ± SD. Significance determined by one-way ANOVA with Tukey's post hoc test (A, K, L) or two-tailed unpaired Student's t-test (E, H) (*P < 0.05, **P < 0.01, ***P < 0.001, ****P < 0.0001). Results shown are from one of at least three independent replicates; all experiments produced comparable data.

4. Mobilization of glycogen storage to fuel luteal steroidogenesis during the avascular phase

To test whether the stored glycogen in GCs is used to fuel the avascular CL for steroidogenesis, we augmented glycogen storage during glycogenesis phase via 2g/kg dose of glucose (glucose tolerance dose) administration (Figure 4A-C). By 15 hours post-hCG (H15), the glucose-loaded luteinizing GCs exhibited reduced NAD^+/NADH ratio, increased ATP generation, upregulated luteal gene expression and increased progesterone secretion compared to the controls (Figure 4D, E; S5A). This functional enhancement persisted until H40 (Figure S5B), indicating the glycogen storage as a critical determinant of luteal function.

To further validate the functional importance of glycogen, RNA interference was performed to suppress the glycogen synthesis. *In vitro* knockdown of glycogenesis genes *Ugp2* and *Gys1* did not impair follicular development and ovulation but markedly reduced GC glycogen storage in pre-ovulatory follicles (Figure 4F, G; S6A-C). This intervention precipitated a profound bioenergetic crisis at H15, characterized by increased NAD^+/NADH ratio, diminished MMP, reduced ATP generation, significantly suppressed progesterone synthesis and luteal gene expression (Figure 4H-J; S6D, E). *In vivo* ovarian bursa delivery of *Ugp2* and *Gys1* interference plasmids (Figure 4K-M; S7A) recapitulated this bioenergetic crisis with: increased NAD^+/NADH, decreased ATP, downregulated luteal gene expression and reduced serum progesterone (Figure 4N-P; S7B).

Complementarily, inhibition of glycogen catabolism during the glycogenolysis phase using the PYGB inhibitor–Ingliforib (Figure 4Q, R) also induced luteal insufficiency, evidenced by decreased ATP production, downregulated luteal gene expression and attenuated progesterone synthesis in the glycogen-constrained luteinizing GCs (Figure 4S, T; S7C).

To definitively investigate the functional necessity of glycogen storage *in vivo*, the GC-specific *Gys1* conditional knockout mice (cKO-*Gys1*) were generated using a

Gyp19a1-Cre driver system (Figure 4U; S7D). This genetic ablation abolished glycogen accumulation within GCs of the mice (Figure 4V). Concomitantly, cKO mice exhibited significant bioenergetic perturbation in their avascular CLs, including elevated NAD^+/NADH ratio, impaired ATP production and significantly suppressed progesterone synthesis along with attenuated luteal gene expression at H15 (Figure 4W, X; S7E). Moreover, cKO mice displayed a significant decrease in litter size compared to *Gys1*$^{floxp/floxp}$ (Figure 4Y).

These data confirm that glycogenesis in GCs establishes an essential energy reservoir, which mobilized during the avascular phase to fuel the bioenergetic demands of progesterone production in nascent CL. This cellular adaptive mechanism hereafter termed GCES.

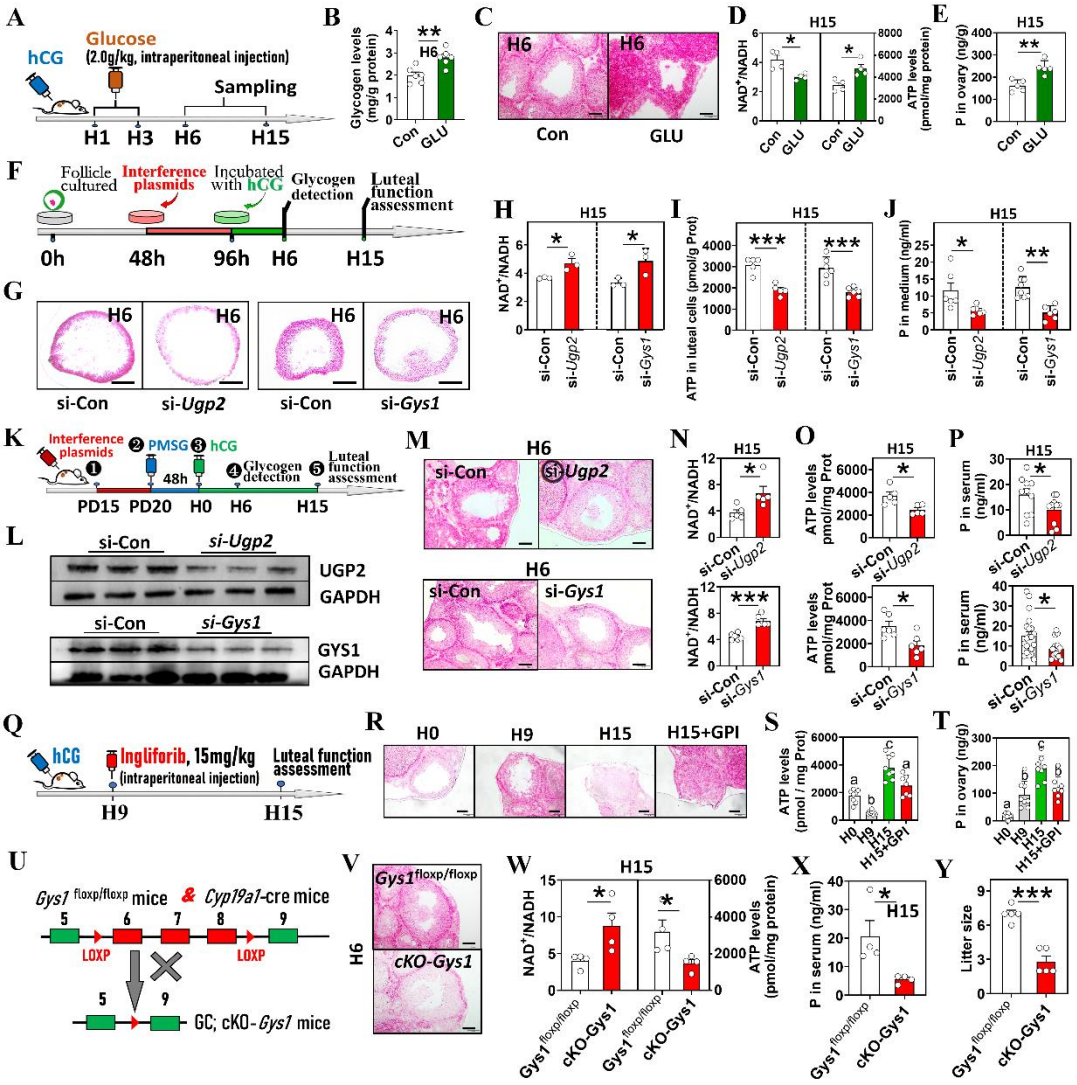

Figure 4. Mobilization of glycogen storage to fuel luteal steroidogenesis during the avascular phase. (A) Experimental design for panels (B-E). (B) Colorimetric quantification of glycogen content in GC post-glucose injection (n = 6 GC samples). (C) PAS staining of glycogen storage post-glucose injection; scale bar = 100 μm. (D) Alterations in NAD^+/NADH

ratio and ATP contents post-glucose injection (n = 4 GC samples). (E) Progesterone levels in ovarian homogenates measured by radioimmunoassay post-glucose injection (n = 5 ovarian samples). (F) Experimental design for *Ugp2*/*Gys1* knockdown in cultured mouse follicles. Luteinizing GCs isolated at H15 for functional assessment. (G) Changes in GC glycogen storage post-*Ugp2* and *Gys1* knockdown. The commercial scrambled siRNA serving as si-Control (si-Con). Scale bar = 100 μm. (H) Alterations in NAD^+/NADH in GCs post-knockdown; n = 3 GC samples. (I) ATP content in GCs post-knockdown (n = 5-6 GC samples). (J) Progesterone in culture medium post-knockdown (n = 6-8 samples). (K) Experimental design for in vivo lentiviral-mediated *Ugp2*/*Gys1* knockdown. Luteinizing GCs isolated from CLs at H15 for functional assessment. (L) Western blotting confirmation of *Ugp2*/*Gys1* knockdown in ovaries (n = 3 ovarian samples). (M) PAS staining of glycogen storage post-knockdown. Scale bar = 100 μm. (N) NAD^+/NADH alterations in GCs post-knockdown (n = 5-6 GC samples). (O) ATP content changes in GCs post-knockdown (n = 5-6 GC samples). (P) Progesterone level alterations post-knockdown; n = 10 (si-*Ugp2*), 15-21 (si-*Gys1*) serum samples. (Q) Experimental design for Ingliforib treatment in vivo. (R) PAS staining validation of Ingliforib-mediated glycogenolysis inhibition. Scale bar = 100 μm. (S) ATP levels in luteinizing GCs post-Ingliforib treatment (n = 7-8 GC samples). (T) Progesterone in ovarian homogenates post-Ingliforib treatment (n = 8 ovarian samples). (U) Schematic representation of the conditional knockout of *Gys1* in mouse GCs. (V) PAS staining of glycogen storage in GCs post-knockout. Scale bar = 100 μm. (W) Alterations in NAD^+/NADH ratio and ATP contents (n = 4 GC samples). (X) Progesterone level alterations post-knockout (n = 4 serum samples). (Y) Litter size alterations post-knockout (n = 5 mice). Data represent mean ± SD. Significance determined by two-tailed unpaired Student's t-test or one-way ANOVA with Tukey's post hoc test (S, T) (*P < 0.05, **P < 0.01, ***P < 0.001). Results shown are from one of twice (V-Y) or at least three (A-T) independent replicates; all experiments produced comparable data.

5. hCG (LH) induces glycogen storage via MAPK-RUNX1-Insulin signaling axis

To identify the intracellular signaling regulating GCES, KEGG enrichment analysis was performed. The results showed a significant induction of insulin signaling during early luteinization (Figure 5A). Consistent with this, qRT-PCR and Western blotting demonstrated that hCG injection markedly increased both mRNA and protein levels of insulin/IGF-1 receptors (INSR and IGF1R) in GCs, concomitant with enhanced receptor phosphorylation (Figure 5B; S8A). Functional validation demonstrated that insulin alone was sufficient to enhance glucose uptake and glycogen storage in GCs. Conversely, pharmacological inhibition of INSR/IGF1R with BMS536924 abolished hCG-induced glucose uptake and glycogen storage (Figure 5C-F), confirming the necessity of insulin signaling for hCG-driven glycogen storage.

We next investigated mechanism by which hCG (LH) initiates insulin signaling. In addition to insulin signaling, the significant induction of the MAPK (ERK1/2) signaling during early luteinization was also observed with KEGG analysis (Figure 5A). Among the transcription factors potently induced by hCG, RUNX1–a known downstream target of MAPK–was ranked relatively higher (Figure 5G, H). Moreover, publicly available ChIP-seq data [23] indicated specific binding of RUNX1 to *Igf1r* and *Insr* promoters

350 (Figure 5I). Taken together, these data collectively suggest that hCG activates insulin
351 signaling via the MAPK-RUNX1 cascade. To test this, the C16-PAF was used to active
352 MAPK signaling. This treatment recapitulated the effects of hCG supplementation
353 including RUNX1 upregulation, insulin signaling activation and glycogen accumulation
354 in GCs. Conversely, MAPK inhibition with U0126 abolished all these effects induced by
355 hCG (Figure 5J, K).

356 To identify whether there is a direct transcriptional regulation between RUNX1 and
357 insulin/IGF-1 receptors, both electrophoretic mobility shift assays (EMSA) and chromatin
358 immunoprecipitation quantitative PCR (ChIP-qPCR) were performed. EMSA confirmed
359 the specific RUNX1 binding sites with the predicted consensus motifs within the *Igf1r*
360 and *Insr* promoters (Figure 5L; S8B-D). ChIP-qPCR confirmed an increased RUNX1
361 occupancy at these promoter regions at H6 (Figure 5M). Site-directed mutagenesis
362 localized the RUNX1 response element to the TGTGGT motif in both promoters (Figures
363 5N; S8E). Finally, RUNX1 knockdown in cultured follicles suppressed hCG-induced
364 insulin signaling activation and glycogen storage in GCs (Figures 5O-Q; S8F).

365 These results demonstrate that glycogen storage stimulated by hCG (LH) in GCs
366 is mediated via MAPK-RUNX1-Insulin signaling axis.

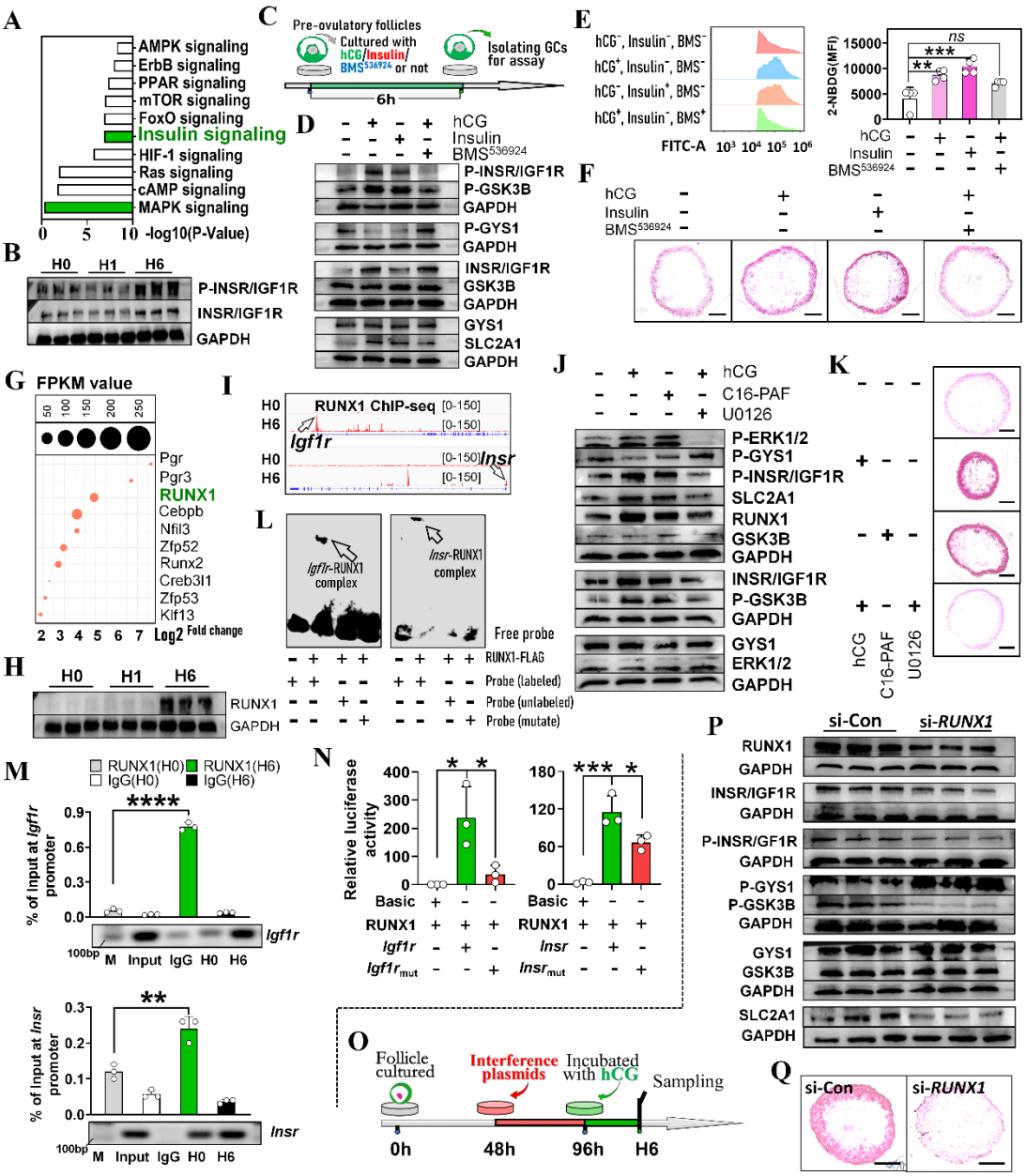

Figure 5. hCG (LH) induces glycogen storage via MAPK-RUNX1-Insulin signaling axis. (A) KEGG pathway analysis of signaling activation in GCs post-hCG injection. (B) Western blotting analysis of INSR/IGF1R activity in GCs post-hCG injection (n = 3 GC samples). (C) Experimental design for panels (D-F). (D) Western blotting analysis of glycogenesis related proteins in GCs after insulin pathway modulation. (E) Flow cytometric analysis of glucose uptake capacity in GCs. Left: representative images; Right: quantification. Isolated GCs were incubated with fluorescent analog 2-NBDG for 30 minutes prior to analysis (n = 4 GC samples). (F) PAS staining of glycogen stores in GCs after insulin signaling manipulation. Scale bar = 100 μm. (G) Top 10 transcription factors upregulated in GCs by hCG (bubble plot). (H) Western blotting analysis of RUNX1 expression in GCs post-hCG injection (n = 3 GC samples). (I) ChIP-seq profiles of RUNX1 binding at *Igf1r* and *Insr* promoters. Arrows: enrichment peaks. (J) Western blotting analysis of RUNX1 and glycogenesis related proteins in GCs after MAPK pathway modulation. (K) PAS staining of glycogen stores after MAPK pathway modulation. Scale bar = 100 μm. (L) EMSA validating RUNX1 binding to *Igf1r* and *Insr* promoter motifs. (M) ChIP-qPCR quantification of RUNX1 binding to *Igf1r* and *Insr* promoters (n = 3 GC

samples). (N) Dual-luciferase reporter assays identifying RUNX1-responsive elements in *Igf1r* and *Insr* promoters (n = 3 cellular samples). (O) Experimental design for panels (P, Q). (P) Western blotting analysis of glycogenesis regulators in GCs post-RUNX1 knockdown (n = 3 GC samples). (Q) PAS staining of glycogen stores after RUNX1 knockdown. Scale bar = 100 μm. Data represent mean ± SD. Significance determined by one-way ANOVA with Tukey's post hoc test (*P < 0.05, **P < 0.01, ***P < 0.001, ****P < 0.0001). Results shown (B-F, H, J-Q) are from one of at least three independent replicates; all experiments produced comparable data.

6. GCES augmentation enhanced luteal function and pregnancy outcomes in mouse and ovine models

To assess the clinical relevance of GCES, glycogen storage in mouse GCs was augmented with timely glucose administration (Figures 6A, B). This intervention significantly elevated progesterone levels by gestation day 15 (GD15; Figure 6C). Crucially, the progesterone-enhancing effect of glucose administration was contingent exclusively into the glycogenesis phase; glucose administration outside this temporal window was proved no effective (Figure S9A). Compared to controls, the glucose-treated mice exhibited a reduced fetal regression rate (Figure 6D), increased fetal and placental weights (Figure 6E), although fetal number remained unchanged (Figure 6D). To critically evaluate the functional relevance to assisted reproduction, we further assessed the impact of glucose administration on the farrowing rate following embryo transfer (Figure 6F). Glucose treatment during the temporal window significantly increased the farrowing rate compared to the control group (Figure 6G), demonstrating its potential utility in reproductive technologies.

The functional conservation of GCES was also investigated in sheep, a mono-ovulatory species. Similar to the mouse model, LH injection significantly upregulated the expression of genes involved in insulin and glycogenesis pathway, reduced ATP generation and increased glycogen accumulation in sheep GCs (Figures 6H, I; S9B, C). The subsequent glucose potentiation (1.5g/kg, aligned with human glucose tolerance dose) further increased glycogen storage (Figures 6I, J), concomitantly elevating progesterone levels and luteal gene expression by GD20 (Figure 6K; S9D). Strikingly, the pregnancy rate was significantly higher in the glycogen-augmented group (81.25%) compared to controls (63.45%; $p < 0.01$, Figure 6L).

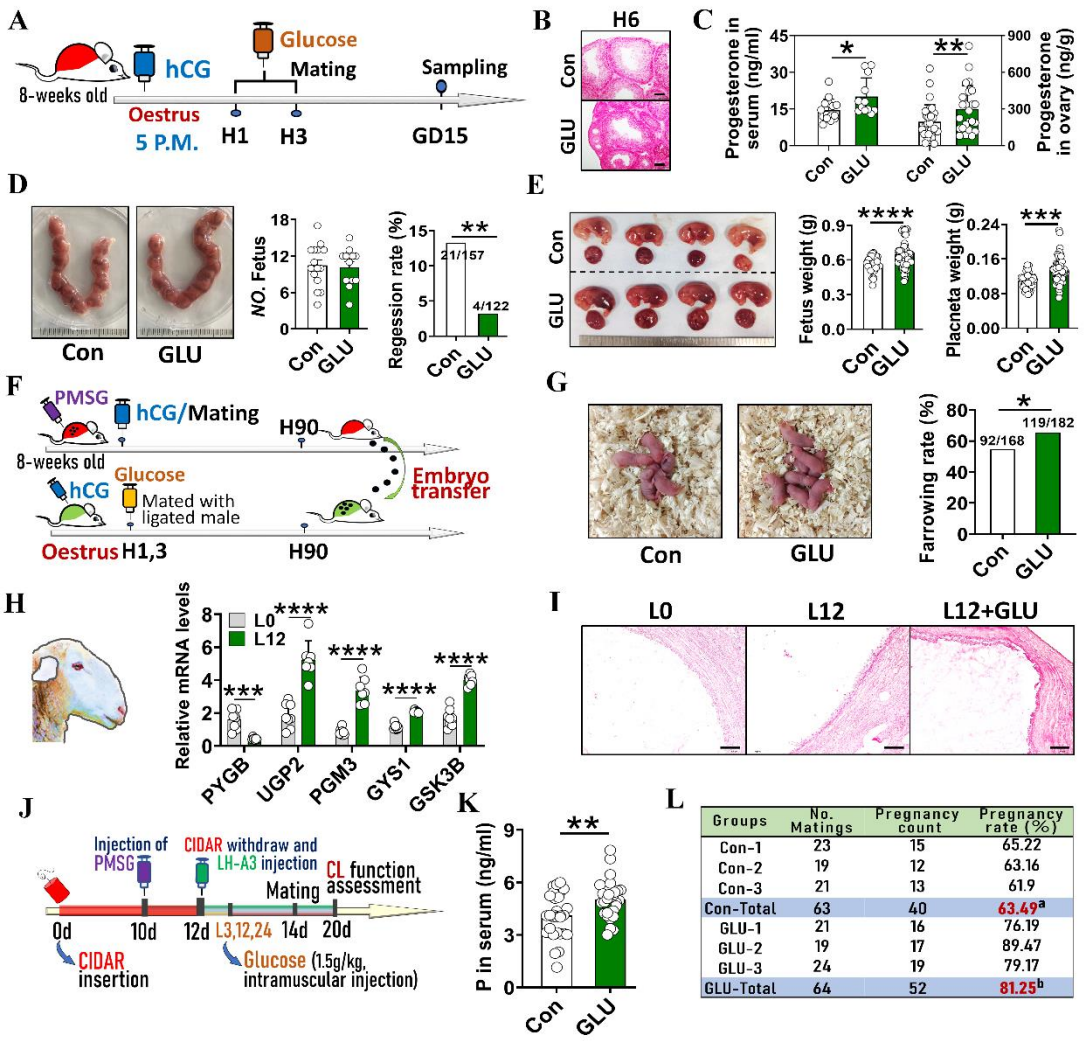

Groups	No. Matings	Pregnancy count	Pregnancy rate (%)
Con-1	23	15	65.22
Con-2	19	12	63.16
Con-3	21	13	61.9
Con-Total	63	40	63.49[a]
GLU-1	21	16	76.19
GLU-2	19	17	89.47
GLU-3	24	19	79.17
GLU-Total	64	52	81.25[b]

Figure 6. GCES augmentation enhanced luteal function and pregnancy outcomes in mouse and ovine models. (A) Experimental design for panels B to E. (B) PAS staining of glycogen. Scale bar = 100 µm. (C) Effects of glucose intake on serum and ovarian progesterone levels at GD15; n (serum) = 15 (Con), 12 (GLU); n (ovarian homogenate) = 30 (Con), 24 (GLU). (D) Effects of glucose intake on fetal number and regression rates at GD15 (n = 15 pregnant mice). (E) Effects of glucose intake on fetal and placental weights at GD15; n = 4 (Con) and 5 (GLU) pregnant mice. (F) Embryo transfer experimental schematic. (G) Effects of glucose intake on the farrowing rate of transferred embryos. (H) qRT-PCR analysis of glycogen metabolism genes in ovine GCs pre-(L0) and 12 hours post-LH injection (L12); n = 8 (L0), 7 (L12) GC samples. (I) PAS staining of glycogen in ovine GCs post-LH injection. Scale bar = 500 µm. (J) Experimental design for panels I to L. (K) Effects of glucose intake on serum progesterone levels (n = 30 serum samples). (L) Effects of glucose intake on sheep pregnancy rate after breeding. Data represent mean ± SD. Significance determined by two-tailed unpaired Student's t-test or chi-square test (D, G and L) (*P < 0.05, **P < 0.01, ***P < 0.001, ****P < 0.0001). Results shown are from one of at least three independent replicates; all experiments produced comparable data.

433 **7. Timely oral glucose administration enhances GCES and luteal function in**
434 **humans**

435 Transitioning to humans, the transcriptome of human GCs following hCG
436 administration was analyzed by using public databases [33]. GO analysis revealed the
437 enrichment of these hCG-downregulated genes in high-energy-demanding processes
438 and ATP production, similar to the findings in mouse and ovine models (Figure 7A).
439 Moreover, the expression of glucose transporters *SLC2A13*, *SLC2A14* and *SLC2A3*
440 exhibited a sharp increase at H12, returning to baseline by H32 (Figure 7B).
441 Furthermore, hCG administration significantly upregulated insulin signaling
442 components, including *IGF1R*, *IGFBP1*, *IGFBP3*, *IGFBP5* and *IRS2* (Figure 7C),
443 supporting the evolutionary conservation of GCES mechanisms in humans.

444 To translate these findings clinically, we recruited volunteers undergoing assisted
445 reproductive technology (ART). Participants were instructed orally intake of 75g
446 glucose (glucose tolerance dose) at 12 hours post-hCG trigger. Their progesterone
447 synthetic capacity was assessed 24 hours post-glucose ingestion (Figure 7D). This
448 timely oral glucose administration significantly augmented glycogen storage within
449 human GCs (Figure 7E). Compared to the control group, the glucose-treated group
450 demonstrated significantly upregulated expression of luteal genes in luteinizing GCs
451 (Figure 7F), culminating in a ~73% increase ($p < 0.001$) in mean progesterone
452 concentration within follicular fluid (Figure 7G).

453 These results demonstrate that a single, timely oral glucose intervention following
454 hCG trigger significantly elevates glycogen reserves in human GCs and increases
455 progesterone production.

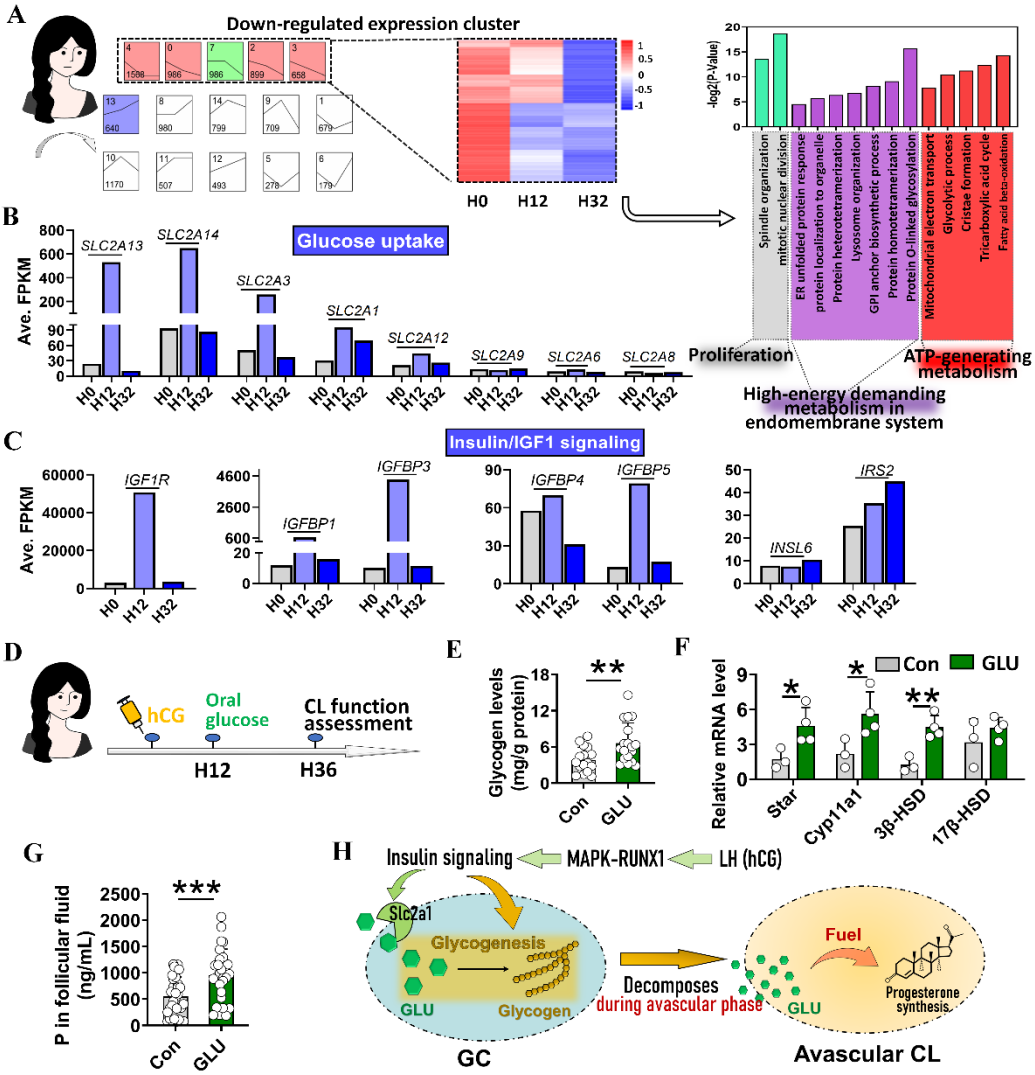

Figure 7. Timely oral glucose administration enhances GCES and luteal function in humans. (A) GO enrichment analysis of the downregulated expression cluster in human GCs post-hCG injection. Left: heatmap; Right: enriched GO terms. (B) Expression of glucose transporter genes in GCs post-hCG injection. (C) Expression of insulin pathway genes in GCs post-hCG injection. (D) Experimental design for panels E to G. Volunteers were randomly selected from women undergoing ART treatment and responding normally to controlled ovarian hyperstimulation. (E) Colorimetric qualification of glycogen storage in GCs post-glucose intake; n = 16 (Con), 18 (GLU) GC samples. (F) qRT-PCR analysis of luteal gene expression post-glucose intake; n = 3 (Con), 4 (GLU) GC samples. (G) Progesterone levels in follicular fluids measured by radioimmunoassay post-glucose intake; n = 34 (Con), 28 (GLU) samples. (H) A diagram depicting GCES. Data represent mean ± SD. Significance determined by two-tailed unpaired Student's t-test (*P < 0.05, **P < 0.01, ***P < 0.001). The experiments (E, G) were repeated twice with consistent results.

470 **DISCUSSION**

471 The acquisition of progesterone synthesis capacity precedes the vascularization in the
472 CL. How does the avascular CL meet the substantial bioenergetic demands for the high
473 level of progesterone production is still unknown. Our study resolves this enigma by
474 identifying GCES as the key mechanism. We demonstrate that during early
475 luteinization, hCG (LH) orchestrates a metabolic transition in GCs via the MAPK-
476 RUNX1-Insulin signaling axis, redirecting glucose toward glycogenesis. This
477 strategically stored glycogen is subsequently mobilized to fuel intensive progesterone
478 production throughout the avascular phase, ensuring normal luteogenesis (Figure 7H).
479 The GCES process fundamentally refines our understanding of luteinization. This
480 process strikingly parallel to oocyte nutrient provisioning for preimplantation embryos
481 [34] highlights conserved regulatory strategies in reproduction. Moreover, GCs emerge
482 as a novel insulin-sensitive glycogenic cell type, distinct from hepatocytes and
483 myocytes [35,36], with broad physiological implications.

484 GCES not only serves as an energy source for avascular CL but also profoundly
485 influencing mature luteal function (Figure S5B), indicating significant translational
486 promise. GCES enhancement improved luteal function in both polytocous (mice) and
487 monotocous (sheep) species, leading to marked increases in pregnancy rates. In human
488 trials, the timely oral glucose administration induces the GCES enhancement,
489 increasing progesterone content by ~73%. Crucially, this GCES-mediated luteal
490 support was achieved solely through glucose intake, bypassing pharmaceutical agents,
491 thereby being exceptional safety. This is particularly significant since no treatment for
492 luteal insufficiency has been reported to improve pregnancy rates in natural menstrual
493 cycle [3]. Therefore, we propose a novel preconception strategy: peri-ovulatory intake
494 of glucose or high-glycemic-index foods (such as cakes, milk tea, candies) as a potential
495 means to mitigate luteal insufficiency and improve fertility outcomes. Given its safety,
496 accessibility, transit use and cost-effectiveness, this approach promises broad adoption
497 in populations with a higher incidence of luteal insufficiency, potentially reducing
498 reliance on conventional luteal phase support–especially in women who experience the
499 dual risk factors of early pregnancy bleeding and a history of one or more previous
500 miscarriages [37,38].

501 In livestock production, GCES-based luteal enhancement could integrate
502 seamlessly with estrus synchronization and embryo transfer to boost pregnancy rates

503 and reduce infertility or miscarriage attributable to luteal deficiency, as validated in
504 sheep (Figure 6K, L; S9D). Importantly, optimal implementation requires precision
505 timing, dosage (the dose employed herein was glucose tolerance dose), and frequency
506 of glucose administration. Murine data identified a ≤9-hour post-hCG window (marked
507 by glucose transporter/glycogen synthase upregulation) for effective glucose
508 intervention. Extra-window supplementation fails to improve luteal function (Figure
509 S9A), necessitating species-tailored glucose regimens–a key challenge in clinical
510 translation.

511 While GCs and theca cells jointly contribute to luteogenesis, GO analysis revealed
512 a distinct metabolic divergence. Unlike GCs, theca cells neither enter metabolic quiesce
513 nor accumulate glycogen following luteinization initiation (Figure S10A-D). Thus,
514 glycogen storage represents a GC-specific adaptation. Intriguingly, theca cells exhibit
515 significantly higher glycogen content compared to other follicular cell types during
516 folliculogenesis (Figure S10E), suggesting that theca cells may also engage in glycogen
517 storage, albeit initiating this process earlier than GCs.

518 In summary, this study introduces the novel concept of GCES and demonstrates
519 that enhancing GCES via timely glucose administration improves luteal function in
520 different species including humans. These insights advance reproductive physiology
521 and hold substantial promise for developing novel therapeutic approaches to address
522 luteal insufficiency in both livestock and human clinical translation.

523 **LIMITATIONS**

524 While we have identified the LH (hCG)-MAPK-RUNX1-Insulin axis regulating
525 glycogen storage in GCs, the signaling pathway(s) inducing metabolic quiescence
526 remains undefined. Beyond elevated energy demands, robust progesterone production
527 also requires substantial cholesterol precursor, yet how the developing CL maintains
528 cholesterol supply during its avascular phase has not been investigated. Furthermore, the
529 mandatory progesterone supplementation following embryo transfer in ART protocols
530 [39,40] precludes direct assessment of GCES-mediated improvement in pregnancy
531 outcomes of humans. Future studies should aim to: (i) delineate the mechanisms
532 governing GC metabolic quiescence and cholesterol provision, and (ii) quantify the
533 effects of GCES enhancement on pregnancy rates in natural conception cohorts.

534 **MATERIALS AND METHODS**

535 **Experimental design**

536 This study commenced with the prediction of GC metabolic alterations during early
537 luteinization using multi-omics profiling. These predictions were experimentally
538 validated, defining a novel cellular adaptive mechanism, GCES. The functional
539 impact of GCES on luteogenesis was then investigated through targeted
540 manipulation in vitro and in vivo. Meanwhile, the regulatory pathway controlling
541 GCES was elucidated. Finally, the translational potential of GCES was evaluated
542 across species and in a preliminary clinical setting.

543 (1) **Multi-Omics Profiling of GC Dynamics during Early Luteinization**: Integrated
544 single-cell and spatial transcriptomics analysis was performed to delineate high-
545 resolution transcriptional profiles of GCs within pre-ovulatory follicles at 0, 1, and
546 6 hours post-hCG administration, simulating the LH surge. Subsequent GO
547 enrichment analysis of transcriptomic profiles predicted metabolic alterations in
548 GCs during early luteinization, revealing attenuated high-energy demanding and
549 ATP-generating activities alongside enhanced insulin responsiveness and glucose
550 homeostasis.

551 (2) **Experimental Validation of Metabolic Alterations**: Next, a multi-modal approach
552 was employed to validate the omics-derived predictions, encompassing: targeted
553 metabolomics, electron microscopy, flow cytometry, mitochondrial functional
554 assays, glucose uptake capacity measurements, isotopic tracing, qRT-PCR, Western
555 blotting, immunofluorescence, PAS staining, and enzymatic activity assays. This
556 validation confirmed that GCs enter a metabolically quiescent state while
557 concurrently enhancing glucose uptake and conversion to glycogen for storage, *i.e.*
558 GCES.

559 (3) **Functional Impact of GCES on luteinization**: To investigate whether GCES
560 governs luteal function by modulating energy availability during the avascular
561 phase, glycogen storage was manipulated assessed both in vitro and in vivo via: (i)
562 glucose supplementation to enhance glycogen storage; (ii) RNA interference and
563 conditional knockout strategies to block glycogen storage; and (iii)
564 pharmacological inhibition of glycogen catabolism. The functional consequences

565 of these interventions on luteal energy supply and progesterone biosynthesis were
566 rigorously evaluated.
567 (4) **Validation of GCES Regulatory Pathway**: Bioinformatics-driven analyses,
568 coupled with flow cytometry, pharmacological modulation (inhibitors/activators),
569 RNA interference, Western blotting, EMSA, ChIP-qPCR, luciferase reporter assay,
570 and PAS staining, were utilized to elucidate the signaling pathway(s) governing
571 GCES.
572 (5) **Translational Evaluation of GCES in a Three-Phase Approach**: (i) The
573 conservation of the GCES phenomenon was validated across species (mouse, sheep,
574 human); (ii) The impact of augmenting GCES via post-hCG glucose administration
575 on luteal function, pregnancy rate, and embryo transfer success was systematically
576 evaluated in mouse/ovine models; (iii) Volunteers undergoing ART treatment were
577 recruited. Following hCG administration, participants received an oral glucose
578 administration at 12 hours to augment GCES. The efficacy of this intervention in
579 enhancing early human luteal function was assessed.

580 **Animals**

581 KM strain mice were sourced from the Center for Animal Testing at Huazhong
582 Agricultural University (Wuhan, China), while *Gys1*$^{floxp/floxp}$ C57BL/6J mice [41] were
583 obtained from GemPharmatech (Nanjing, China). GC-specific deletion of *Gys1* exons
584 6-8 was achieved by crossing *Gys1*$^{floxp/floxp}$ mice with Cyp19a1-Cre transgenic mice [42]
585 (Cyagen; Suzhou, China). All mice were maintained under specific pathogen-free (SPF)
586 conditions with controlled temperature (25 ± 1°C), a 12-hour light/dark cycle, and ad
587 libitum access to food and water. Sheep subjects were housed at Xinjiang Jinken Aoqun
588 Agriculture and Animal Husbandry Technology (Hetian, China) following standard
589 husbandry protocols. Experimental procedures strictly adhered to the institutional
590 guidelines for laboratory animal welfare and were approved by the Animal Ethics
591 Committee of Huazhong Agricultural University (Approval No.: HZAUMO-2023-
592 0115; HZAUSH-2024-0001).

593 **Human clinical trials**

594 Female participants (25-40 years) undergoing ART treatment were prospectively

595 enrolled in this clinical study. Following comprehensive verbal and written disclosure
596 of study objectives, procedures, and potential risks/benefits, written informed consent
597 was obtained from all subjects. At 12 hours post-hCG trigger (Ovidrel®, 250 μg; Sigma,
598 USA), participants were instructed to ingest 75g glucose (Chinaotsuka, China).
599 Transvaginal ultrasound (Voluson™ P8; GE Healthcare, USA)-guided follicular
600 aspiration was performed at 36 hours post-hCG administration to collect luteinizing
601 GCs and follicular fluid from mature pre-ovulatory follicles (16-22 mm diameter). GCs
602 were immediately processed for glycogen quantification and luteal gene expression
603 profiling, while follicular fluid was centrifuged (3,000 ×g, 10 minutes) for subsequent
604 progesterone quantification. The study protocol, designed in accordance with
605 Declaration of Helsinki principles, received prior approval from the Institutional
606 Review Board of Renmin Hospital, Wuhan University (Approval No.: WDRY2024-
607 K262), with continuous monitoring ensuring strict adherence to ethical safeguards
608 regarding patient autonomy and biological sample handling.

609 **Superovulation**

610 Mouse superovulation was induced via intraperitoneal administration of 5 IU pregnant
611 mare serum gonadotropin (PMSG; NSHF, China), followed by 5 IU hCG (NSHF, China)
612 48 hours post-PMSG administration to trigger follicle maturation and subsequent
613 ovulation/luteinization. In sheep, estrus synchronization was achieved through
614 intravaginal insertion of progesterone-impregnated controlled internal drug release
615 (CIDR) devices (Zoetis, USA). Following 10 days of CIDR priming, ewes received 400
616 IU PMSG via intramuscular injection. CIDR removal at 12 days post-insertion
617 coincided with 12.5 μg LH-A3 (NSHF, China) administration to induce
618 ovulation/luteinization. Three timely subcutaneous glucose injections (1.5 g/kg body
619 weight) were administered at 3, 12 and 18 hours post-LH-A3 treatment. Post-mating
620 evaluation included luteal functional assessment through serum progesterone
621 quantification 6 days post-mating and ultimate pregnancy confirmation via
622 ultrasonography (Kxele, China) 30 days post-conception.

623 **Transcriptome analysis**

624 While single-cell RNA-seq enables high-resolution transcriptomic characterization of
625 GCs, its temporal accuracy diminishes in discriminating pre-ovulatory follicle GCs
626 across discrete post-hCG intervals. Conversely, spatial transcriptomics preserves
627 locational fidelity but lacks the resolution of single-cell RNA-seq. To synergize these
628 complementary modalities, we established a spatiotemporal transcriptomic atlas of
629 mouse GCs through multi-omics integration. Mouse ovaries were collected at H0, H1
630 and H6 for single-cell RNA-seq (Yingzi Gene, China). Following cell viability
631 assessment (>85%) and density calibration (1,000 cells/μL), single-cell suspensions
632 were processed on the 10 × Chromium Single Cell Platform (10 × Genomics), involving
633 gel beads in emulsion (GEM) generation, reverse transcription, cDNA amplification,
634 and Illumina-compatible library preparation. Libraries were quantified via Qubit
635 Fluorometry (Thermo, USA) and sequenced on the Illumina Nova6000 platform
636 (Illumina, USA) using 150-base-pair paired-end reads. Raw sequencing data underwent
637 primary analysis using Cell Ranger (v2.1.), performing demultiplexing, genome
638 alignment (GRCm38), Unique Molecular Identifier (UMI), and quality filtering. To
639 reduce dimensionality, the top ten principal components were utilized, and t-Distributed
640 Stochastic Neighbor Embedding (tSNE) was employed. Cell clustering was achieved
641 through a graph-based clustering algorithm, involving the construction of a sparse
642 nearest-neighbor graph followed by Louvain Modularity Optimization [43].
643 Differential gene expression analysis between cell clusters was conducted using the
644 Seurat Bimod test, with significance thresholds set at a false discovery rate (FDR) ≤
645 0.05 and an absolute log2 fold change ≥ 1.5. Spatial transcriptomic data from mouse
646 ovaries were retrieved from the Gene Expression Omnibus (GEO) database
647 (GSE240271), with processed metadata and cell annotation files obtained from the
648 associated GitHub repository (https://github.com/madhavmantri/mouse_ovulation).

649 The integrative analysis commenced with single-cell RNA-seq data preprocessing,
650 where sequencing depth variability was mitigated through total UMI count
651 normalization using *scanpy.pp.normalize_total*. Spatial cell-type mapping was
652 achieved via a PyTorch-implemented deep neural network

653 (*tangram.map_cells_to_space*), trained over 2,000 epochs (learning rate=0.01, Adam
654 optimizer) on 220 ovary-specific marker genes under RNA count-based spatial
655 constraints (*Density_prior='rna_count_based'*). Model optimization targeted
656 minimization of Kullback-Leibler divergence between single-cell RNA-seq and spatial
657 transcriptomic datasets. Cellular annotations (*Subclass_label*) were projected onto
658 spatial coordinates through probabilistic embedding (*tg.project_cell_annotations*), with
659 dominant spot-level cell types resolved via maximum likelihood estimation
660 (*tangram_ct_pred*). Integrated transcriptomes were generated using *tg.project_genes*,
661 followed by multi-level quality control: (i) Training convergence: Visualized via loss
662 function trajectories (*tg.plot_training_scores*); (ii) Cross-platform consistency:
663 Quantified through pairwise gene expression correlation (*tg.plot_genes_sc*); (iii)
664 Spatial fidelity: Validated via AUC metrics for marker gene colocalization
665 (*tg.compare_spatial_geneexp*). Finally, the temporal expression dynamics of genes in
666 GCs post-hCG were profiled using STEM (Short Time-series Expression Miner) with
667 hierarchical clustering (Euclidean distance, complete linkage).
668 Human transcriptome data was extracted from the GEO database, with login
669 numbers GSE133868. GO enrichment analysis of genes was performed through
670 DIAVD database (https://david.ncifcrf.gov/tools.jsp). KEGG enrichment analysis of
671 genes were performed through KOBAS database (http://kobas.cbi.pku.edu.cn/home.d).

672 **Follicle culture**

673 Small antral follicles (250-300 μm diameter) were micro dissected from mouse ovaries
674 using 33-gauge precision needles (KONSFI, China) and subsequently cultured
675 individually in 96-well round bottom cell culture plates (Bkmbio, 110303005, China)
676 under standard conditions (37°C, 5% CO_2, humidified atmosphere). Follicle culture
677 medium consisted of α-MEM (Gibco, C12571500BT, USA) supplemented with 5%
678 FBS (Serana, FBS-AS500, Germany), 1% ITS-G (Thermo, 41400045, USA), 10
679 mIU/mL rFSH (GONAL-f®; sigma, USA), and 100 U/mL penicillin-streptomycin
680 (Servicebio, G4003, China). Following 96 hours of culture, follicles reaching the pre-
681 ovulatory stage were transitioned to high-glucose luteinization induction medium. This

682 medium consisted of α-MEM supplemented with 5mg/mL D-Glucose (MCE, HY-
683 B0389, USA), 1.5 IU/mL rhCG (Ovidrel®; Sigma, USA), 1ng/mL Prolactin (MCE,
684 HY-P700292, USA), 10 μM Cholesterol (MCE, HY-N0322, USA), 1% ITS-G, 5% FBS,
685 10 mIU/mL rFSH, 10 ng/mL hEGF (Thermo, AF-100-15, USA), and 100 U/mL
686 penicillin/streptomycin.

687 **RNA interference**

688 Lentivirus-mediated RNA interference was implemented to achieve targeted gene
689 silencing in follicles or whole ovaries. Gene-specific small interfering RNAs (siRNAs)
690 targeting *Ugp2* (5′-GCAAACTGAGACTGGTGGAAA-3′), *Gys1* (5′-
691 GCCCATGTCTTCACTACCGTA-3′), and *RUNX1* (5′-CGGCAGAACTGAGAAATGCTA-3′)
692 were designed and synthesized by Genepharma (Suzhou, China), with a commercial
693 non-targeting siRNA (MISSION®; Sigma, USA) serving as the negative control. Next,
694 siRNA sequences were cloned into the PLKO.1-EGFP-PURO plasmid (Genecreate,
695 China) under the human U6 promoter. For lentiviral packaging, HEK293T cells (ATCC,
696 USA) were co-transfected in 6-well plates with three plasmids: 0.89 μg siRNA-
697 expressing PLKO.1-EGFP-PURO, 0.44 μg pMD2.G (VSV-G envelope; Addgene,
698 USA), and 0.67 μg pSPAX2 (packaging plasmid; Addgene, USA) using 4 μL
699 jetPRIME® transfection reagent (PolyPlus, 101000046, France). Viral supernatants
700 were harvested 48 hours post-transfection, filtered through 0.45 μm Polyvinylidene
701 Fluoride (PVDF membranes; Sigma, IPVH00010, USA), and clarified by
702 ultracentrifugation (100,000 ×g, 2 hours; Beckman, USA).

703 For in vitro gene knockdown, the isolated small antral follicles were transfected
704 with lentiviral particles (titer: 6.25×10^8 particles/mL) in follicle culture medium
705 supplemented with 10 μg/mL Polybrene (Sigma, TR-1003-G, USA) for 48 hours (37°C,
706 5% CO_2). Transfection was confirmed by EGFP fluorescence visualization. Transfected
707 follicles were subsequently cultured for 48 hours to reach the pre-ovulatory stage,
708 followed by transfer to high-glucose luteinization medium for terminal stimulation.
709 Samples were collected at predefined intervals for analysis.

710 For in vivo ovarian-specific knockdown, fifteen-day-old mice were anesthetized

711 with 1% pentobarbital sodium (50 mg/kg; Sigma, USA). A total of 5 μL high-titer
712 lentivirus (titer: 6.25 × 10^9 particles/mL) was bilaterally microinjected beneath the
713 ovarian bursa using a Hamilton 701N syringe (10 μL capacity; 80330, Switzerland)
714 coupled to a 33-gauge RN needle (Hamilton, 7803-05, Switzerland). Control cohorts
715 received equivalent volumes of non-targeting siRNA lentivirus. Mice were allowed to
716 recover for 5 days prior to experimental analyses to ensure stable gene knockdown.

717 **Metabolic flux assay**

718 Pre-ovulatory follicles (550-600 μm diameter) were micro dissected from mouse
719 ovaries and preconditioned in glucose-depleted Dulbecco's Modified Eagle Medium
720 (DMEM; Gibco, 11966-025, USA) for 2 hours to deplete endogenous glucose.
721 Following depletion, follicles were cultured for 6 hours in luteinization medium
722 containing 2 mg/mL uniformly labeled $^{13}C_6$-glucose (^{13}C-glucose; MCE, HY-B0389A,
723 USA) to achieve isotopic labeling of glycolytic intermediates. Metabolic flux analysis
724 was performed by Biotree (Shanghai, China). GCs isolated from the follicles underwent
725 cryogenic homogenization in liquid nitrogen, followed by suspension in 1 mL of pre-
726 chilled (−40°C) 50% methanol. After two sequential freeze-thaw cycles (dry ice/ice
727 bath), phase separation was achieved by adding 0.4 mL chloroform with vigorous
728 vortexing (30 sec) and centrifugation (12,000 ×g, 15 minutes, 4°C). The polar
729 metabolite-enriched aqueous phase was analyzed via hydrophilic interaction liquid
730 chromatography (HILIC) on an XBridge BEH Amide column (150 × 2.1 mm, 2.5 μm;
731 Waters, USA) coupled to a Q Exactive™ Plus Orbitrap mass spectrometer (Thermo,
732 USA) operated in negative electrospray ionization (ESI^-) mode. Chromatographic
733 gradient employed: solvent A (20 mM NH_4Ac/NH_4OH in water:acetonitrile, 95:5) and
734 solvent B (acetonitrile). Gradient program: 0-3 minutes (10% A, 90% B), 3-8 minutes
735 (25% A, 75% B), 8-10 minutes (30% A, 70% B), 10-13 minutes (50% A, 50% B), 13-
736 16 minutes (75% A, 25% B), 16-20.5 minutes (100% A, 0% B), 20.5-25 minutes (10%
737 A, 90% B) at a flow rate of 0.15 mL/minutes and column temperature of 25°C. Mass
738 spectrometric parameters included: Resolution, 140,000 (at m/z 200); Automatic gain
739 control (AGC) target, 1 × 10^6 ions; scan range, m/z 75–1000; Column temperature:

740 25°C. ^{13}C-isotopologue distributions were deconvoluted using El-MAVEN v.12.0,
741 incorporating MATLAB (v2021b)-based algorithms for natural isotopic abundance
742 correction to enable quantitative determination of metabolic flux through central carbon
743 pathways.

744 **Quantification of ^{13}C-Glucose incorporated into glycogen**

745 The isolated pre-ovulatory follicles were preconditioned in glucose-depleted DMEM
746 for 2 hours. Subsequently, follicles were incubated for 6 hours in luteinization medium
747 supplemented with 2 mg/mL ^{13}C-glucose to facilitate isotopic incorporation into
748 glycogen. Post-culture, GCs were isolated from follicles, homogenized in ultrapure
749 water, and partitioned into paired aliquots. The experimental aliquot was subjected to
750 acid hydrolysis using 6 M trifluoroacetic acid (TFA; 100°C, 4 hours) to depolymerize
751 glycogen and release bound glucose monomers, while the paired control aliquot
752 remained unhydrolyzed to quantify background glucose levels. Following hydrolysis,
753 samples were equilibrated to ambient temperature (25 ± 1°C) and lyophilized under
754 reduced pressure (300 mbar, 52°C) using a rotary evaporator (Heidolph, Germany).
755 Dried residues were reconstituted in 0.5 M methanolic 1-phenyl-3-methyl-5-
756 pyrazolone (PMP) solution, followed by the addition of an equimolar volume of
757 aqueous ammonia (28%, pH 12.5) to initiate derivatization. The mixture was vortexed
758 and incubated at 70°C for 90 minutes to form glucose-PMP derivatives. Post-
759 derivatization, samples underwent three sequential purification cycles, each involving
760 resuspension in 1 mL ultrapure water followed by rotary evaporation (300 mbar, 40°C)
761 to remove residual ammonia. ^{13}C-glucose-PMP adducts were then extracted via
762 biphasic partitioning (chloroform/water; 1:1 v/v), with the aqueous phase collected for
763 ultra-performance liquid chromatography coupled to quadrupole time-of-flight mass
764 spectrometry (UPLC-QTOF-MS; Waters, USA) analysis. Chromatographic separation
765 was performed on an ACQUITY C18 column (100 × 2.1 mm, 1.7 μm; Waters, USA)
766 maintained at 45°C using a binary gradient consisting of solvent A (0.1% formic acid
767 in water) and solvent B (acetonitrile) at a flow rate of 0.4 mL/minutes. Gradient
768 program: 0-1 minutes (99% A, 1% B); 1-2 minutes (80% A, 20% B); 2-5 minutes (60%

769 A, 40% B); 5-6 minutes (45% A, 55% B); 6-13 minutes (20% A, 80% B); 13-17 minutes
770 (5% A, 95% B); 17-20 minutes (99% A, 1% B). Sample injection volume was 1 μL.
771 Mass spectrometric detection was performed in positive electrospray ionization (ESI^+)
772 mode with a scan range of m/z 50-1200. Instrument parameters included: desolvation
773 gas flow, 500 L/hour at 400°C; cone gas flow, 50 L/hour; source temperature, 100°C;
774 capillary voltage, 1000 V; cone voltage, 30 V; acquisition rate, 0.3 sec with no inter-
775 scan delay. The sample cone voltage was optimized using the instrument's tune page.
776 Accurate mass measurement and elemental composition determination for precursor
777 and fragment ions were conducted using MassLynx 4.1 software (Waters, USA), with
778 ^{13}C-glucose of glycogen calculated as: experimental aliquot ^{13}C-glucose - control
779 aliquot ^{13}C-glucose.

780 **Metabolite analysis**

781 Metabolomic profiling was performed by Majorbio (Shanghai, China). GCs isolated
782 from pre-ovulatory follicles at specified post-hCG timepoints (H0 and H6) were mixed
783 with ice-cold methanol: water (4:1, v/v) extraction solvent (containing 0.02 mg/mL 2-
784 chloro-L-phenylalanine as internal standard). Homogenization used a Wonbio-96c
785 tissue grinder (wonbio, China) at 50 Hz for 6 minutes (-10°C), followed by 30-minutes
786 ultrasonic extraction (5°C, 40 kHz) and centrifugation (13,000 ×g, 15 minutes, 4°C) to
787 collect supernatants for injection. Analysis employed a Thermo Scientific™ Vanquish
788 UHPLC coupled to Q Exactive™ HF-X system (Thermo, USA) with heated
789 electrospray ionization (HESI) source operated in polarity switching mode.
790 Chromatographic separation used an ACQUITY UPLC HSS T3 column (100 mm × 2.1
791 mm, 1.8 μm; Waters, USA) with mobile phase A (0.1% formic acid in water: acetonitrile,
792 2:98) and B (0.1% formic acid in acetonitrile) at 0.4 mL/minutes, column temperature
793 40°C, and injection volume 5 μL. The gradient program was: 0-2 minutes (95%A, 5%B);
794 2-14 minutes (5%A, 95%B); 14-14.1 minutes (95%A, 5%B); 14.1-17 minutes (95%A,
795 5%B). Mass spectrometry parameters: full MS resolution 120,000 (@ m/z 200), dd-
796 MS^2 resolution 30,000 (@ m/z 200), scan range m/z 70-1050, spray voltage +3.5 kV/-
797 2.8 kV, capillary temperature 400°C, sheath gas 40 arb, aux gas 10 arb, S-lens RF 55%.

798 Quality control employed pooled QC samples injected every 10 experimental samples
799 with retention time deviation < 0.1 minutes and peak intensity RSD < 15%. Raw data
800 processing used Progenesis QI v3.0 (Waters, USA) for peak extraction (S/N threshold >
801 3), alignment (5 ppm mass tolerance), and normalization (internal standard correction).
802 Statistical analysis on Majorbio Cloud Platform (https://cloud.majorbio.com), in GPI-
803 anchor biosynthesis pathway annotated using KEGG database (https://www.kegg.jp/).

804 **Analysis of glucose uptake capacity**

805 The glucose uptake capacity of GCs was quantified using the fluorescent D-glucose
806 analog 2-NBDG (MCE, HY-116215, USA). Briefly, GCs were isolated from pre-
807 ovulatory follicles at specified post-hCG timepoints, washed twice with phosphate-
808 buffered saline (PBS; pH 7.4), and resuspended in pre-warmed (37°C) 2-NBDG
809 working solution (100 μM in glucose-depleted DMEM). Following 30-minutes
810 incubation at 37°C under 5% CO_2, GCs were pelleted by centrifugation (600 ×g, 5
811 minutes), washed twice with ice-cold PBS to terminate uptake, and finally resuspended
812 in PBS. Fluorescence intensity of internalized 2-NBDG, which directly correlates with
813 cellular glucose uptake capacity, was measured using a BD FACSAria™ III flow
814 cytometer (BD Biosciences, USA) equipped with a 488-nm laser and 530/30-nm
815 emission filter. 20,000 viable cells *per* sample were acquired. Data analysis was
816 performed using FlowJo v10.4.0 software (BD Biosciences, USA), with results
817 expressed as geometric mean fluorescence intensity (MFI).

818 **Transmission electron microscope**

819 Pre-ovulatory follicles isolated from mouse ovaries at designated post-hCG timepoints
820 were processed for transmission electron microscopy analysis. Follicles were primarily
821 fixed by immersion in 2.5% (v/v) glutaraldehyde (SPI Chem, USA) at 4°C for 12 hours.
822 Subsequently, samples were rinsed thrice with 0.1 M PBS (pH 7.4) and post-fixed with
823 1% (w/v) osmium tetroxide (OsO_4; SPI Chem, USA) in PBS for 2 hours at 4°C.
824 Thereafter, specimens were dehydrated through a graded ethanol series (30%, 50%,
825 70%, 90%, 100%; Sinopharm, China), transitioned to propylene oxide, and infiltrated
826 with Spurr's epoxy resin (SPI Chem, USA) using ascending resin:propylene oxide ratios

827 (1:3, 1:1, 3:1 v/v). Pure resin-embedded samples were polymerized at 60°C for 48 hours.
828 Ultrathin sections (60 nm thickness) were cut using a diamond knife on a Leica UC7
829 ultramicrotome (Leica, Germany), mounted on 200-mesh copper grids, and double-
830 stained with 2% (w/v) uranyl acetate (SPI Chem, USA) for 30 minutes followed by
831 Reynolds' lead citrate for 5 minutes. Ultrastructural examination of GCs was performed
832 using a HT7800 transmission electron microscope (Hitachi, Japan) operated at 80 kV.
833 Digital images were acquired using an CCD camera (Gatan, USA) with standardized
834 exposure settings.

835 **PAS Staining**

836 Glycogen deposition in tissues was assessed using Periodic Acid-Schiff Staining Kit
837 (Sigma, 395B-1KT, USA). According to manufacturer's specifications, ovarian samples
838 were fixed in a 4% paraformaldehyde solution (Servicebio, G1101, China) containing
839 30% sucrose for 48 hours at 4°C. Post-fixation, samples were embedded in Optimal
840 Cutting Temperature (OCT) compound (Sakura, 4583, USA). The cultured follicles
841 were directly embedded in OCT. 6-μm-thick cryosections were prepared using a
842 freezing microtome (Leica, Germany) maintained at -20°C. Sections were washed in
843 PBS (3 × 5 minutes), post-fixed with 4% paraformaldehyde for 20 minutes at room
844 temperature, and rinsed in PBS (3 × 5 minutes). Subsequently, sections were oxidized
845 in periodic acid solution for 10 minutes, rinsed in PBS (5 minutes), stained with Schiff's
846 reagent for 25-30 minutes in the dark, and washed in PBS for 5 minutes. Imaging was
847 performed using a microscope (Olympus, Japan) equipped with a digital camera under
848 200 × magnification.

849 **Immunofluorescence staining**

850 Ovaries collected at designated post-hCG timepoints were fixed in 4%
851 paraformaldehyde for 48 hours at 4°C, dehydrated through graded ethanol series,
852 cleared in xylene, and embedded in paraffin. 3-μm-thick sections were prepared using
853 a rotary microtome (Leica, Germany). Sections were deparaffinized in xylene (2 × 10
854 minutes), rehydrated through descending ethanol gradients, and subjected to heat-
855 induced epitope retrieval in sodium citrate buffer (Solarbio, C1032, China) at 98°C for

856 30 minutes. After cooling to room temperature, sections were blocked with 10% (v/v)
857 normal goat serum (Boster, AR0009, China) in PBS for 60 minutes at room temperature.
858 Subsequently, sections were incubated with rabbit anti-CD34 monoclonal primary
859 antibody (1:300 dilution; Abclonal, A19015, China) diluted in SuperKine™ Enhanced
860 Antibody Dilution Buffer (Abbkine, BMU103, China) for 12 hours at 4°C in a
861 humidified chamber. Following three washes in PBS (5 minutes each), sections were
862 incubated with Alexa Fluor® 594-conjugated goat anti-rabbit IgG secondary antibody
863 (1:200 dilution; Abclonal, AS039, China) for 60 minutes at room temperature protected
864 from light. Nuclei were counterstained with 10 μg/mL 4′,6-diamidino-2-phenylindole
865 (DAPI; Biosharp, BL105A, China) for 10 minutes. After final PBS washes (3 × 5
866 minutes), sections were mounted with antifade mountant (Servicebio, G1401, China)
867 and imaged using a confocal laser scanning microscope (Zeiss, Germany) equipped
868 with 405-nm (DAPI) and 561-nm (Alexa Fluor® 594) lasers. Images were acquired at
869 200 × magnification and processed using ZEN 2.3 lite software (Zeiss, Germany).

870 **Lysosome analysis**

871 Lyso-Tracker Green (Beyotime, C1047S, China) was utilized for lysosome
872 quantification analysis. Following the manufacturer's protocol, GCs were isolated from
873 pre-ovulatory follicles at specified post-hCG timepoints, washed with HBSS (Beyotime,
874 C0218, China). Subsequently, GCs were stained with the Lyso-Tracker Green working
875 solution and incubated at 37°C for 30 minutes. Fluorescence values were measured
876 using a flow cytometry instrument (BD Biosciences, USA), and data analysis was
877 conducted through FlowJo 10.4. GCs with Lyso-tracker (FITC) fluorescence > 3×10^3,
878 defined using a threshold slightly above the negative control maximum, were termed
879 high Lyso-tracker fluorescence GCs.

880 **Analysis of lysosomal acid phosphatase activity**

881 Lysosomal acid phosphatase activity in GCs isolated from pre-ovulatory follicles at
882 designated post-hCG timepoints was determined using an Acid Phosphatase Activity
883 Assay Kit (Boxbio, AKFA017C, China). According to manufacturer’s instructions,
884 GCs were resuspended in 100 μL of lysis buffer and mechanically homogenized.

885 Lysates were centrifuged at 8,000 ×g for 10 minutes at 4°C to obtain supernatants.
886 Aliquots (20 μL) of the supernatant were incubated with ACP working solution for 15
887 minutes at 37°C. Following enzymatic reactions, ACP chromogenic substrate was
888 added and the mixture was incubated at room temperature for 10 minutes to develop
889 color. Absorbance at 510 nm were measured using a Spark Multimode Microplate
890 Reader (Tecan, Switzerland). Enzymatic activities were calculated from a 6-point
891 standard curves (0.5-8.0 μmol/mL) and expressed as U per g protein, with protein
892 concentrations determined via bicinchoninic acid (BCA) assay kit (Servicebio, G2026,
893 China).

894 **MMP assay**

895 MMP was quantified using a JC-1-based Mitochondrial Membrane Potential Assay Kit
896 (Solarbio, M8650, China). According to manufacturer's instructions, isolated GCs were
897 resuspended in pre-warmed (37°C) assay buffer and incubated with 10 μM JC-1
898 working solution for 20 minutes at 37°C under 5% CO_2 in the dark. Subsequently, cells
899 were pelleted by centrifugation (600 ×g, 10 minutes), washed twice with ice-cold JC-1
900 staining buffer, and resuspended in fresh assay buffer. Fluorescence intensities were
901 measured using the Spark Multimode Microplate Reader with the following settings:
902 excitation/emission = 485/535 nm (green monomeric form) and 535/590 nm (red J-
903 aggregates). MMP was expressed as the ratio of red (590 nm) to green (535 nm)
904 fluorescence intensity, where decreased ratios indicate mitochondrial depolarization.

905 **ATP quantification**

906 ATP levels in GCs were quantified using an ATP Determination Kit (Thermo, A22066,
907 USA) based on firefly luciferase chemiluminescence. According to manufacturer's
908 instructions, isolated GCs were lysed in 60 μL ice-cold ATP extraction buffer by
909 homogenizing followed by 5-minutes incubation on ice. Lysates were centrifuged
910 (10,000 ×g, 4°C, 5 minutes) to remove insoluble debris. Background ATP in 96-well
911 opaque plates (Corning, 3915, USA) was quenched by incubating with 100 μL ATP
912 detection working solution for 5 minutes at room temperature. Subsequently, 20 μL
913 supernatant of cell lysates was mixed with 100 μL ATP detection working solution.

914 Chemiluminescence signals (relative light units, RLU) were immediately measured
915 using the Spark Multimode Microplate Reader. ATP concentrations were interpolated
916 from a 6-point standard curve (0-0.64 nmol/mL) and normalized to total protein content,
917 with results expressed as pmol/mg protein.

918 **Quantification of NAD^+/NADH ratio**

919 The NAD^+/NADH ratio in GCs was determined using a NAD^+/NADH Assay Kit
920 (Beyotime, S0175, China) based on alcohol dehydrogenase (ADH)-coupled WST-8
921 reduction. According to manufacturer's instructions, GCs were lysed in 120 μL ice-cold
922 extraction buffer and centrifuged (10,000 ×g, 4°C, 10 minutes). For total NAD
923 (NAD^++NADH) quantification, 20 μL supernatant was mixed with 90 μL NADH
924 working solution and 10 μL WST-8 chromogen, then incubated at 37°C for 30 minutes.
925 For NADH-specific quantification, an identical aliquot was heated at 60°C for 30
926 minutes to decompose NAD^+ prior to reagent addition. Post-decompose, 20 μL
927 supernatant was mixed with 90 μL ADH working solution and 10 μL WST-8 chromogen,
928 then incubated at 37°C for 30 minutes. Absorbance at 450 nm was measured using the
929 Spark Multimode Microplate Reader. NAD^+ and NADH concentrations were
930 interpolated from an 8-point NADH standard curve (0-8 nmol/mL), with NAD^+
931 calculated as: Total NAD - NADH. Results were normalized to total protein
932 concentration.

933 **Quantification of glycogen, free fatty acids and triglycerides**

934 GCs isolated from pre-ovulatory follicles at designated post-hCG timepoints were
935 analyzed for glycogen, free fatty acids, and triglycerides using standardized
936 biochemical assays. Glycogen content was determined with a Glycogen Assay Kit
937 (Solarbio, BC0340, China) based on enthrone colorimetric method. According to
938 manufacturer's instructions, GCs were homogenized in extraction buffer, sonicated (35%
939 amplitude, 10 sec pulse × 3; Sonics & Materials Inc, USA), and boiled for 20 minutes.
940 After centrifugation (10,000 ×g, 4°C, 10 minutes), 60 μL supernatant was mixed with
941 240 μL detection buffer and incubated in boiling water for 10 minutes. The absorbance
942 at 620 nm was measured using the Spark Multimode Microplate Reade. Free fatty acids

943 were measured using a Free Fatty Acid Quantification Kit (Boxbio, AKFA008C, China)
944 based on copper soap colorimetry. GCs were homogenized in lysis buffer and
945 centrifuged (10,000 ×g, 4°C, 10 minutes). The supernatant was mixed with extraction
946 buffer by vortexing for 10 minutes. After centrifugation (3,000 ×g, 25°C, 10 minutes),
947 the supernatant was mixed with detection buffer and incubated in room temperature for
948 10 minutes. Absorbance at 550 nm was measured against palmitic acid standards (0.05-
949 1.00 μmol/mL). Triglyceride content was assessed via Triglyceride Assay Kit (Njjcbio,
950 A110-1-1, China) employing GPO-PAP methodology: GCs were lysed in RIPA buffer
951 containing 1 × protease/phosphatase inhibitor (Proteintech, PR20038, China), sonicated
952 (35% amplitude, 10 sec pulse × 3), and centrifuged (10,000 ×g, 4°C, 15 minutes). 10
953 μL supernatant was mixed with 200 μL enzymatic working solution and incubated at
954 37°C for 10 minutes. Absorbance was measured at 500 nm. All values were normalized
955 to total protein, with results expressed as mg/g protein (Glycogen), μmol/g protein (Free
956 Fatty Acids and triglyceride).

957 **Progesterone determination**

958 Serum, follicular fluid and culture medium samples were clarified by centrifugation
959 (3,000 ×g, 4°C, 10 minutes), while ovarian tissues were homogenized in ice-cold PBS
960 and centrifuged (10,000 ×g, 4°C, 10 minutes). Resulting supernatants were aliquoted
961 and stored at -80°C until analysis. Progesterone concentrations were quantified via
962 radioimmunoassay (RIA) performed by Beijing North Institute of Biological
963 Technology, a certified clinical testing laboratory (Beijing, China) using a commercial
964 RIA kit with validated sensitivity (2 pg/mL). The assay employed competitive binding
965 between endogenous progesterone and ^{125}I-labeled progesterone tracer for anti-
966 progesterone polyclonal antibody binding sites. Following 1 hour incubation at 37°C,
967 antibody-bound fractions were separated using polyethylene glycol precipitation.
968 Radioactivity was measured for 1 minute per tube in a γ-counter (PerkinElmer, USA).
969 Standard curves (0-100 ng/mL) were established with each run, and ovarian
970 progesterone levels were normalized to tissue weight (ng progesterone/g ovarian tissue).

971 **Pharmaceutical intervention protocols**

972 All compounds were procured from MCE. Stock solutions were prepared according to
973 manufacturers' specifications and diluted in appropriate vehicles immediately prior to
974 use. In vivo inhibition of glycogenolysis: Ingliforib (HY-19396) dissolved in 10%
975 DMSO/90% corn oil was administered via intraperitoneal injection (100 μL, 15 mg/kg)
976 9 hours post-hCG injection. In vitro modulation: 40 nM insulin (HY-P0035) was
977 supplemented into the luteinization medium to activate insulin signaling, while 100 nM
978 BMS-536924 (HY-10262) was used to suppress this signaling. MAPK pathway was
979 activated by 10 μM C16-PAF (HY-108635), whereas suppressed by 40 μM U0126 (HY-
980 12031A). All compounds were filter-sterilized (0.22 μm; Sigma, SLGV004SL, USA)
981 and controls included equivalent vehicles.

982 **Western blotting**

983 Total proteins were extracted using RIPA lysis buffer (Thermo, 89901, USA)
984 supplemented with 1 × protease/phosphatase inhibitor and 1 mM PMSF (Thermo,
985 36978, USA) on ice. Lysates were centrifuged (10,000 ×g, 4°C, 15 minutes) and
986 supernatants quantified via BCA assay kit. Equal protein loads (20 μg/lane) were
987 resolved on SDS-polyacrylamide gels at 80 V (stacking) and 120 V (resolving) in Tris-
988 Glycine-SDS buffer (25 mM Tris, 250 mM glycine, 0.1% SDS, pH 8.3) and transferred
989 to 0.45 μm PVDF membranes at 72 V for 100 minutes in transfer buffer (48 mM Tris,
990 39 mM glycine, 0.037% SDS, 10% methanol). Membranes were blocked with 5% non-
991 fat dry milk (Nestlé, Switzerland) in TBST (Servicebio, G0004, China) for 1 hour at
992 room temperature, then incubated overnight at 4°C with primary antibodies diluted in
993 SuperKine™ Enhanced Antibody Dilution Buffer: phospho-PKCα (CST, #9375,
994 1:1000), SLC2A1 (Proteintech, 21829-1-AP, 1:1000), GYS1 (CST, #3886, 1:1000),
995 GSK3B (CST, #12456, 1:1000), phospho-GYS1 (CST, #47043, 1:1000), phospho-
996 GSK3β (CST, #9323, 1:1000), PYGB (Proteintech, 12075-1-AP, 1:1000), UGP2
997 (Proteintech, 10391-1-AP, 1:800), INSR/IGF1R (Abclonal, A21984, 1:1000), phospho-
998 INSR/IGF1R (CST, #3024, 1:800), RUNX1 (Proteintech, 25315-1-AP, 1:1000),
999 ERK1/2 (Abclonal, A4782, 1:1000), phospho-ERK1/2 (CST, #9101, 1:1000), GAPDH

1000 (Abclonal, AC002, 1:5000). After TBST washes (3 × 10 minutes), membranes were
1001 incubated with species-matched HRP-conjugated secondary antibodies (goat anti-
1002 rabbit IgG, BF03008; goat anti-mouse IgG, BF03001; Biodragon, 1:4000) for 1 hour at
1003 25°C. Following TBST washes (3 × 10 minutes), signals were developed with
1004 SuperSignal™ West Pico PLUS Chemiluminescence Kit (Thermo, 34580, USA) and
1005 captured using a Tanon-5200 Chemiluminescence Imager (Biotanon, China).
1006 Uncropped blots are presented in Supplementary Figure S11.

1007 **Lectin binding assay**

1008 For lectin blotting, GCs collected at H0, H1 and H6 were homogenized in ice-cold
1009 PIERCE™ IP Lysis Buffer (Thermo, 87787, USA) supplemented with 1 ×
1010 protease/phosphatase inhibitor and 1 mM PMSF. Lysates were incubated at 4°C for 30
1011 minutes with end-over-end rotation, then centrifuged at 10,000 ×g for 15 minutes at
1012 4°C. Supernatants were quantified using BCA assay kit. Equal protein was resolved on
1013 SDS-polyacrylamide gels at 80 V (stacking) and 120 V (resolving) in Tris-Glycine-SDS
1014 buffer and transferred to 0.45 μm PVDF membranes at 72 V for 100 minutes in transfer
1015 buffer. Membranes were blocked with 1 × Carbo-Free™ Blocking Solution (Vector,
1016 SP-5040, USA) for 1 hour at 25°C with agitation, then incubated with 1 μg/mL
1017 Biotinylated-Concanavalin A (MCE, HY-NP0174, USA)/Biotinylated-Peanut
1018 Agglutinin (MCE, HY-NP0182, USA) in blocking buffer for 1 hour at 25°C. After
1019 TBST washes, membranes were probed with Streptavidin-HRP (Thermo, N100; 1:4000
1020 dilution in blocking buffer) for 1 hour at 25°C. Following additional TBST washes,
1021 signals were developed using SuperSignal™ West Pico PLUS Chemiluminescent
1022 Substrate and captured using a Tanon-5200 Chemiluminescence Imager with automatic
1023 gain control. Full uncropped blots are provided in Supplementary Figure S11.
1024 For lectin flow cytometry assay, GCs were isolated from H0, H1 and H6 ovaries and
1025 washed twice with ice-cold PBS. Cells were incubated with FITC labeled MALI
1026 (Vector, FL-1311, USA)–20 μg *per* 10^6 cells concentration in 1 × Carbo Free blocking
1027 buffer for 20 minutes at room temperature. Finally, cells were diluted to 10^6/mL using
1028 1 × Carbo Free blocking buffer and analyzed using a Cytek® Aurora Full Spectrum

1029 Flow Cytometry (Cytek, USA) equipped with a 488-nm laser and 520-nm emission
1030 filter. 10,000 viable cells *per* sample were acquired. Data analysis was performed using
1031 FlowJo v10.4.0 software, with results expressed as geometric MFI.

1032 **EMSA protocol**

1033 Mouse RUNX1 coding sequence (NCBI RefSeq: NM_001111021) was cloned into
1034 pcDNA3.1-3XFlag plasmid (Addgene, China) for eukaryotic expression. Flag-tagged
1035 RUNX1 protein was immunoprecipitated from HEK293T cell lysates using anti-Flag
1036 M2 affinity gel (Sigma, A2220, USA) with three wash cycles in TBST. Bound proteins
1037 were eluted with 0.1 M glycine (pH 2.7) and immediately neutralized with a
1038 neutralization buffer (1 M Tris, pH 8.5). JASPAR web-based platform
1039 (https://jaspar.elixir.no/) was employed to predict the direct binding sites of RUNX1
1040 within the promoter regions of the *Insr* and *Igf1r*. Based on the predicted motifs,
1041 double-stranded DNA probes and corresponding site-directed mutant probes were
1042 designed, and subsequently synthesized by Genecreate (Wuhan, China). EMSA was
1043 conducted using a Chemiluminescent EMSA Kit (Beyotime, GS009, China). According
1044 to manufacturer's instructions, biotinylated double-stranded DNA probes containing
1045 consensus RUNX-binding motifs were incubated with purified Flag-RUNX1 (100 ng)
1046 in binding buffer for 30 minutes at room temperature. Protein-DNA complexes were
1047 resolved on 6% non-denaturing polyacrylamide gels (29:1 acrylamide:bis) in TBE
1048 buffer (Beyotime, R0223, China) at 100 V for 60 minutes at 4°C. Electrophoretically
1049 transferred to Hybond-N^+ membranes (Cytiva, RPN1510B, USA) at 380 mA for 45
1050 minutes in TBE buffer, complexes were UV-crosslinked (120 mJ/cm², 60 ses), after
1051 blocking with the streptavidin-HRP working solution, the shift-band was detected using
1052 ECL chemiluminescent reagent by exposure on a Tanon-5200 Chemiluminescence
1053 Imager. The probe sequences are provided in Table S2.

1054 **Luciferase reporter assay**

1055 The promoter regions of *Insr* (chr8: 3,171,461-3,172,061 bp) and *Igf1r* (chr7:
1056 67,600,075-67,602,575 bp) were PCR-amplified from mouse genomic DNA and
1057 inserted into the PGL3-Basic luciferase reporter vector (Promega, USA) using the

1058 ClonExpress Ultra One Step Cloning Kit (Vazyme, C115-01, China). Site-directed
1059 mutagenesis of RUNX1-binding motifs (core sequence: 5′-TGTGGT-3′→5′-TGTAGT-
1060 3′) was performed using Mut Express II Fast Mutagenesis Kit (Vazyme, C214-01,
1061 China) with verification by sanger sequencing. HEK293T cells seeded in 24-well plates
1062 (1×10^5 cells/well) were transfected after 24 hours using jetPRIME® reagent with the
1063 following plasmid ratio per well: 250 ng pGL3-*Insr*/pGL3-*Igf1r* (wild-type or mutant),
1064 250 ng RUNX1-pcDNA3.1 or empty vector, and 2.5 ng pRL-TK Renilla*luciferase
1065 control vector (Promega, USA). After 24-hours incubation, cells were lysed in 100 μL
1066 Passive Lysis Buffer and analyzed using the Dual-Luciferase Reporter Assay System
1067 (Promega, E1910, USA). Firefly luciferase activity was measured first using the Spark
1068 Multimode Microplate Reader, followed by Renilla luciferase quantification after Stop
1069 & Glo® reagent addition. Promoter activity was expressed as Firefly/Renilla
1070 luminescence ratio normalized to empty vector control. Primers are listed in
1071 Supplementary Table S2.

1072 **SEAP reporter assay**

1073 A codon-optimized SEAP gene sequence [44] was cloned into the pCDH-CMV-MCS-
1074 EF1-copGFP-T2A-Puro plasmid (GeneCreate, China), followed by lentiviral
1075 packaging in HEK293T cells and concentration by ultracentrifugation to obtain high-
1076 titer lentivirus. Small antral follicles were transfected with lentivirus (titer: 6.25×10^9
1077 particles/mL) to overexpress SEAP, with successful transfection confirmed by EGFP
1078 fluorescence. Upon reaching the pre-ovulatory stage, follicles were transferred to
1079 luteinization medium for 6 hours. Next, GCs were isolated by mechanical dissection
1080 and cultured in fresh follicle medium for another hour. Following centrifugation (3,000
1081 ×g, 10 minutes, 4°C), the GC pellets were lysed in RIPA buffer for BCA assay, while
1082 the supernatants were aspirated for SEAP assay using Phospha-Light™ SEAP Reporter
1083 Assay kit (Thermo, T1015, USA). According to manufacturer's instructions, the
1084 supernatants were diluted 1:1 in 1 × dilution buffer, heat-inactivated at 65 ± 0.5°C for
1085 30 minutes, cooled to 25°C, then 50 μL sample mixed with 50 μL assay buffer (5
1086 minutes, 25°C), followed by 50 μL reaction substrate (20 minutes, 25°C in dark).

1087 Chemiluminescence (relative light units, RLU) was measured using the Spark
1088 Multimode Microplate Reader. SEAP activity was normalized to total protein content.

1089 **qRT-PCR assay**

1090 Total RNA was isolated using TRIzol™ Reagent (Takara, 9109, Japan) and quantified
1091 with a NanoDrop 2000 spectrophotometer (Thermo, USA). Reverse transcription was
1092 performed with 1 μg total RNA using Evo M-MLV RT Kit with gDNA clean (AGbio,
1093 AG11728, China) in 20 μL reactions (37°C for 15 minutes, 85°C for 5 sec). qPCR was
1094 conducted in triplicate on a CFX384/96 Touch™ Real-Time PCR System (Bio-Rad,
1095 USA) with 10 μL reaction volumes containing: 5 μL SYBR Green Premix Pro Taq HS
1096 (AGbio, AG11739, China), 4 μL cDNA template and 250 nM gene-specific primers (1
1097 μL). Thermal cycling parameters: initial denaturation at 95°C for 15 minutes; 35 cycles
1098 of 95°C for 10 sec and 60°C for 30 sec (combined annealing/extension); followed by
1099 melt curve analysis (60°C to 95°C, increment 0.5°C/5 sec). Specificity was confirmed
1100 by single-peak melt curves of PCR products. Relative mRNA expression was calculated
1101 by the $2^{-\Delta\Delta Ct}$ method using *Actb* or *Gapdh* as endogenous controls. Amplified products
1102 were visualized through agarose gel electrophoresis (80V, 80 mA, 75 minutes). The
1103 primer sequences are provided in Table S2.

1104 **ChIP-qPCR assay**

1105 ChIP-qPCR was performed using GCs isolated from pre-ovulatory follicles at specified
1106 post-hCG intervals (H0, H6). Cells were fixed in 10 mL DMEM/F-12 (Gibco,
1107 11320033, USA) containing freshly prepared 1% formaldehyde (CST, 12606S, USA)
1108 for 10 minutes at room temperature with rotation (15 rpm). Fixation was quenched by
1109 adding 1 mL 1.5 M glycine followed by 5 minutes rotation. Cell pellets were washed
1110 thrice with ice-cold PBS in 1.5 mL centrifuge tubes (Axygen, MCT-150-C, USA), then
1111 lysed in pre-chilled cytomembrane lysis buffer (10 mM HEPES pH 7.9, 0.5% IGEPAL-
1112 CA630, 1.5 mM $MgCl_2$, 10 mM KCl, 1 × protease inhibitor cocktail [Abclonal,
1113 RM02916, China]) for 15 minutes at 4°C with vortex agitation (10 sec/5 minutes
1114 interval). Nuclear lysis was conducted in pre-chilled buffer (0.5% SDS, 10 mM EDTA,
1115 50 mM Tris-HCl pH 8.1, 1 × protease inhibitor cocktail) for 15 minutes at 4°C.

1116 Chromatin was sonicated using a ultrasonic disintegrator (Bioruptor Plus; Belgium)
1117 with 30 sec ON/30 sec OFF cycles (30 cycles total) in 4°C water bath to generate 200-
1118 500 bp fragments validated by agarose electrophoresis. Sonicated lysates were
1119 centrifuged at 10,000 ×g for 2 minutes at 4°C, and supernatants diluted 1:10 in ChIP IP
1120 buffer (0.01% SDS, 1% Triton X-100, 2 mM EDTA, 50 mM Tris-HCl pH 8.0, 150 mM
1121 NaCl, 1 × protease inhibitor cocktail). For immunoprecipitation, pre-cleared chromatin
1122 was incubated with 5 μg anti-RUNX1 antibody (Proteintech, 25315-1-AP, China) or
1123 species-matched IgG control (Abcam, ab172730, UK) conjugated to protein A/G
1124 Dynabeads (Thermo, 26162, USA) with rotation overnight at 4°C. The beads were
1125 washed, eluted, and reverse cross-linked. DNA purification was performed using the
1126 QIAquick® PCR Purification Kit (QIAGEN, 28104, Germany). Subsequently, the
1127 DNA was utilized for qPCR analysis with specific primers. Amplified products were
1128 visualized through agarose gel electrophoresis (80V, 80 mA, 75 minutes). The primer
1129 sequences are detailed in Table S2.

1130 **Embryo transfer**

1131 Donor female mice (KM strain, 8 weeks) underwent superovulation and mating with
1132 fertile males. Concurrently, recipient females (8 weeks) in estrus were identified via
1133 vaginal smears [45] and paired with vasectomized males. Vaginal plug confirmation at
1134 08:00 the following morning designated gestational day (GD) 0.5. Donors were
1135 euthanized at GD 3.5 (96 hours post-hCG), and blastocysts were flushed from uterine
1136 horns using KSOM embryo culture medium (Sigma, MR-101, USA) maintained at
1137 37°C under 5% CO_2. Pseudopregnant recipients were anesthetized with 1%
1138 pentobarbital sodium. Six morphologically intact blastocysts per uterine horn were
1139 surgically transferred into each uterine horn using a glass transfer pipette (Jitianbio,
1140 JT0061, China). Muscle and skin layers were closed with absorbable sutures (sh-
1141 Jinhuan, R611 6-0, China). Live birth outcomes were recorded daily from GD 19 until
1142 delivery completion.

1143 **Statistics analysis**

1144 Statistical analyses were using GraphPad Prism 10.0 (GraphPad). Data were expressed
1145 as the mean ± SD. Two-tailed unpaired Student's t test and one-way analysis of variance
1146 followed by Tukey's post hoc test were used to analyze the statistical significance
1147 between two groups and among multiple groups, respectively. Chi-squared test was
1148 used in the comparison between the percentages. The statistical significance was set at
1149 P-value < 0.05. Most experiments were repeated thrice for reproducibility. The number
1150 of experimental replicates is indicated in the corresponding figure legend. If no number
1151 is listed, the experiment was conducted once.

1152 **DATA AVAILABILITY**

1153 The single-cell RNA-seq data reported in this study have been deposited in the GEO
1154 database under accession number GSE297300. All data are available from the
1155 corresponding author upon reasonable request.

1156 **FUNDING**

1157 This research was supported by the Biological Breeding-Major Projects in National
1158 Science and Technology, Grant/Award Number: 2023ZD04049; Fundamental
1159 Research Funds for the Central Universities (2662023DKPY001) and the National
1160 Natural Science Foundation of China (31701301).

1161 **SUPPORTING INFORMATION**

1162 This article contains supporting information.

1163 **ACKNOWLEDGEMENTS**

1164 We extend our deepest appreciation and respect to Mrs. Fu Bijun, Dr. He's mother,
1165 for her genuine care and encouragement throughout this project.

1166 **AUTHORS' CONTRIBUTION**

1167 C.H. conceived, designed, performed, funded the experiments, analysis the data, and
1168 wrote the manuscript; J.L., Q.L., C.L., G.L., and X.L. anticipated in experiment design
1169 and conduction, data analysis, and manuscript preparation; X.W., Y.W., R.L., H.W.,

H.S., Y.Z., W.K., Z.R., Z.W., B.T., C.W., X.J., Q.W., G.H and S.Z assisted with sample collection and experiments conduction; C.H., J.L., Q.L., C.L., G.L., and X.L. revised this manuscript. H.C., G.L., and Q.X. supervised this project. All authors approved the final version.

DECLARATION OF INTERESTS

The authors declare that they have no conflicts of interest with the contents of this article.

REFERENCES

1. Niswender, G. D., Juengel, J. L., McGuire, W. J., Belfiore, C. J., & Wiltbank, M. C. (1994). Luteal function: the estrous cycle and early pregnancy. Biology of reproduction, 50(2), 239–247.
2. Stocco, C., Telleria, C., & Gibori, G. (2007). The molecular control of corpus luteum formation, function, and regression. Endocrine reviews, 28(1), 117–149.
3. Practice Committees of the American Society for Reproductive Medicine and the Society for Reproductive Endocrinology and Infertility (2021). Diagnosis and treatment of luteal phase deficiency: a committee opinion. Fertility and sterility, 115(6), 1416–1423.
4. Dimitriadis, E., Menkhorst, E., Saito, S., Kutteh, W. H., & Brosens, J. J. (2020). Recurrent pregnancy loss. Nature reviews. Disease primers, 6(1), 98.
5. Schliep, K. C., Mumford, S. L., Hammoud, A. O., Stanford, J. B., Kissell, K. A., Sjaarda, L. A., Perkins, N. J., Ahrens, K. A., Wactawski-Wende, J., Mendola, P., & Schisterman, E. F. (2014). Luteal phase deficiency in regularly menstruating women: prevalence and overlap in identification based on clinical and biochemical diagnostic criteria. The Journal of clinical endocrinology and metabolism, 99(6), 1007–1014.
6. Baerwald, A., Vanden Brink, H., Hunter, C., Beuker, D., Lim, H., Lee, C. H., & Chizen, D. (2018). Age-related changes in luteal dynamics: preliminary associations with antral follicular dynamics and hormone production during the human menstrual cycle. Menopause, 25(4), 399–407.
7. Weiss G. (2001). Menstrual irregularities and the perimenopause. Journal of the Society for Gynecologic Investigation, 8(1 Suppl Proceedings), S65–S66.
8. Ellison P. T. (1994). Advances in human reproductive ecology. Annual review of anthropology, 23, 255–275.
9. Salazar, E. L., & Calzada, L. (2007). The role of progesterone in endometrial estradiol- and progesterone-receptor synthesis in women with menstrual disorders and habitual abortion. Gynecological endocrinology : the official journal of the International Society of Gynecological Endocrinology, 23(4), 222–225.
10. Arck, P. C., Rücke, M., Rose, M., Szekeres-Bartho, J., Douglas, A. J., Pritsch, M., Blois, S. M., Pincus, M. K., Bärenstrauch, N., Dudenhausen, J. W., Nakamura, K., Sheps, S., &

Klapp, B. F. (2008). Early risk factors for miscarriage: a prospective cohort study in pregnant women. Reproductive biomedicine online, 17(1), 101–113.

11. Jo, M., Brännström, M., Akins, J. W., & Curry, T. E., Jr (2025). New insights into the ovulatory process in the human ovary. Human reproduction update, 31(1), 21–47.
12. Wang, X., Liao, J., Shi, H., Zhao, Y., Ke, W., Wu, H., Liu, G., Li, X., & He, C. (2024). Granulosa cell-layer stiffening prevents escape of mural granulosa cells from the post-ovulatory follicle. Advanced science, 11(33), e2403640.
13. Monaco, C. F., & Davis, J. S. (2023). Mechanisms of angioregression of the corpus luteum. Frontiers in physiology, 14, 1254943.
14. Curry, T. E., Jr, & Smith, M. F. (2006). Impact of extracellular matrix remodeling on ovulation and the folliculo-luteal transition. Seminars in reproductive medicine, 24(4), 228–241.
15. Goldman, S., & Shalev, E. (2004). MMPS and TIMPS in ovarian physiology and pathophysiology. Frontiers in bioscience : a journal and virtual library, 9, 2474–2483.
16. Robker, R. L., & Richards, J. S. (1998). Hormone-induced proliferation and differentiation of granulosa cells: a coordinated balance of the cell cycle regulators cyclin D2 and p27Kip1. Molecular endocrinology, 12(7), 924–940.
17. Jirawatnotai, S., Moons, D. S., Stocco, C. O., Franks, R., Hales, D. B., Gibori, G., & Kiyokawa, H. (2003). The cyclin-dependent kinase inhibitors p27Kip1 and p21Cip1 cooperate to restrict proliferative life span in differentiating ovarian cells. Journal of biological chemistry, 278(19), 17021–17027.
18. Fan, H. Y., Liu, Z., Johnson, P. F., & Richards, J. S. (2011). CCAAT/enhancer-binding proteins (C/EBP)-α and -β are essential for ovulation, luteinization, and the expression of key target genes. Molecular endocrinology, 25(2), 253–268.
19. Fan, H. Y., Liu, Z., Shimada, M., Sterneck, E., Johnson, P. F., Hedrick, S. M., & Richards, J. S. (2009). MAPK3/1 (ERK1/2) in ovarian granulosa cells are essential for female fertility. Science, 324(5929), 938–941.
20. Wu, Y., Ghosh, S., Nishi, Y., Yanase, T., Nawata, H., & Hu, Y. (2005). The orphan nuclear receptors NURR1 and NGFI-B modulate aromatase gene expression in ovarian granulosa cells: a possible mechanism for repression of aromatase expression upon luteinizing hormone surge. Endocrinology, 146(1), 237–246.
21. Salvador, L. M., Maizels, E., Hales, D. B., Miyamoto, E., Yamamoto, H., & Hunzicker-Dunn, M. (2002). Acute signaling by the LH receptor is independent of protein kinase C activation. Endocrinology, 143(8), 2986–2994.
22. Fan, H. Y., Liu, Z., Cahill, N., & Richards, J. S. (2008). Targeted disruption of Pten in ovarian granulosa cells enhances ovulation and extends the life span of luteal cells. Molecular endocrinology, 22(9), 2128–2140.
23. Dinh, D. T., Breen, J., Nicol, B., Foot, N. J., Bersten, D. C., Emery, A., Smith, K. M., Wong, Y. Y., Barry, S. C., Yao, H. H. C., Robker, R. L., & Russell, D. L. (2023). Progesterone receptor mediates ovulatory transcription through RUNX transcription factor interactions and chromatin remodelling. Nucleic acids research, 51(12), 5981–5996.
24. Meldi, K. M., Gaconnet, G. A., & Mayo, K. E. (2012). DNA methylation and histone modifications are associated with repression of the inhibin α promoter in the rat corpus luteum. Endocrinology, 153(10), 4905–4917.

25. Jeon, H., Choi, Y., Brännström, M., Akin, J. W., Curry, T. E., & Jo, M. (2023). Cortisol/glucocorticoid receptor: a critical mediator of the ovulatory process and luteinization in human periovulatory follicles. Human reproduction, 38(4), 671–685.
26. Pangas S.A., Rajkovic, A. (2015) Chapter 21- follicular development: mouse, sheep, and human Models, in: T.M. Plant, A.J. Zeleznik (Eds.), Knobil and Neill'S Physiology of Reproduction, fourth edition), Academic Press, San Diego, 947–995.
27. Xu, X., Mu, L., Li, L., Liang, J., Zhang, S., Jia, L., Yang, X., Dai, Y., Zhang, J., Wang, Y., Niu, S., Xia, G., Yang, Y., Zhang, Y., Cao, Y., & Zhang, H. (2022). Imaging and tracing the pattern of adult ovarian angiogenesis implies a strategy against female reproductive aging. Science advances, 8(2), eabi8683.
28. Mu, L., Wang, G., Yang, X., Liang, J., Tong, H., Li, L., Geng, K., Bo, Y., Hu, X., Yang, R., Xu, X., Zhang, Y., & Zhang, H. (2025). Physiological premature aging of ovarian blood vessels leads to decline in fertility in middle-aged mice. Nature communications, 16(1), 72.
29. Pereira, M. M., Mainigi, M., & Strauss, J. F. (2021). Secretory products of the corpus luteum and preeclampsia. Human reproduction update, 27(4), 651–672.
30. Mantri, M., Zhang, H. H., Spanos, E., Ren, Y. A., & De Vlaminck, I. (2024). A spatiotemporal molecular atlas of the ovulating mouse ovary. Proceedings of the National Academy of Sciences of the United States of America, 121(5), e2317418121.
31. Rieusset J. (2018). The role of endoplasmic reticulum-mitochondria contact sites in the control of glucose homeostasis: an update. Cell death & disease, 9(3), 388.
32. Chen, J., Zhou, Y., Liu, Z., Lu, Y., Jiang, Y., Cao, K., Zhou, N., Wang, D., Zhang, C., Zhou, N., Shi, K., Zhang, L., Zhou, L., Wang, Z., Zhang, H., Tang, K., Ma, J., Lv, J., & Huang, B. (2024). Hepatic glycogenesis antagonizes lipogenesis by blocking S1P via UDPG. Science, 383(6684), eadi3332.
33. Poulsen, L. C., Bøtkjær, J. A., Østrup, O., Petersen, K. B., Andersen, C. Y., Grøndahl, M. L., & Englund, A. L. M. (2020). Two waves of transcriptomic changes in periovulatory human granulosa cells. Human reproduction, 35(5), 1230–1245.
34. Song, J. L., Wong, J. L., & Wessel, G. M. (2006). Oogenesis: single cell development and differentiation. Developmental biology, 300(1), 385–405.
35. Scoditti, E., Sabatini, S., Carli, F., & Gastaldelli, A. (2024). Hepatic glucose metabolism in the steatotic liver. Nature reviews. Gastroenterology & hepatology, 21(5), 319–334.
36. Hargreaves, M., & Spriet, L. L. (2020). Skeletal muscle energy metabolism during exercise. Nature metabolism, 2(9), 817–828.
37. Devall, A. J., & Coomarasamy, A. (2020). Sporadic pregnancy loss and recurrent miscarriage. Best practice & research. Clinical obstetrics & gynaecology, 69, 30–39.
38. Coomarasamy, A., Devall, A. J., Brosens, J. J., Quenby, S., Stephenson, M. D., Sierra, S., Christiansen, O. B., Small, R., Brewin, J., Roberts, T. E., Dhillon-Smith, R., Harb, H., Noordali, H., Papadopoulou, A., Eapen, A., Prior, M., Di Renzo, G. C., Hinshaw, K., Mol, B. W., Lumsden, M. A., … Gallos, I. D. (2020). Micronized vaginal progesterone to prevent miscarriage: a critical evaluation of randomized evidence. American journal of obstetrics and gynecology, 223(2), 167–176.
39. Carp H. J. A. (2020). Progestogens in luteal support. Hormone molecular biology and clinical investigation, 42(2), 143–148.

40. Garg, A., Zielinska, A. P., Yeung, A. C., Abdelmalak, R., Chen, R., Hossain, A., Israni, A., Nelson, S. M., Babwah, A. V., Dhillo, W. S., & Abbara, A. (2024). Luteal phase support in assisted reproductive technology. Nature reviews. Endocrinology, 20(3), 149–167.
41. Duran J, Saez I, Gruart A, Guinovart JJ, Delgado-García JM. Impairment in long-term memory formation and learning-dependent synaptic plasticity in mice lacking glycogen synthase in the brain. J Cereb Blood Flow Metab. 2013 Apr;33(4):550-6.
42. Fan HY, Shimada M, Liu Z, Cahill N, Noma N, Wu Y, Gossen J, Richards JS. Selective expression of KrasG12D in granulosa cells of the mouse ovary causes defects in follicle development and ovulation. Development. 2008 Jun;135(12):2127-37.
43. Blondel, V. D., Guillaume, J.-L., Lambiotte, R., & Lefebvre, E. (2008). Fast unfolding of communities in large networks. Journal of Statistical Mechanics: Theory and Experiment, 2008(10), P10008.
44. Lowe ME. Site-specific mutations in the COOH-terminus of placental alkaline phosphatase: a single amino acid change converts a phosphatidylinositol-glycan-anchored protein to a secreted protein. J Cell Biol. 1992 Feb;116(3):799-807.
45. Zhang Z, He C, Gao Y, Zhang L, Song Y, Zhu T, Zhu K, Lv D, Wang J, Tian X, Ma T, Ji P, Cui W, Liu G. α-ketoglutarate delays age-related fertility decline in mammals. Aging Cell. 2021 Feb;20(2):e13291.